PHYSICAL REVIEW C VOLUME 20, NUMBER 4 OCTOBER 1979

# States in $^{105,107}$Ag populated by heavy-ion reactions and interpreted by a quasiparticle-plus-rotor model

Rakesh Popli, J. A. Grau,* S. I. Popik,† L. E. Samuelson,‡ F. A. Rickey, and P. C. Simms
*Tandem Accelerator Laboratory, Purdue University, West Lafayette, Indiana 47907*

(Received 7 May 1979)

Levels in $^{105,107}$Ag have been studied using heavy-ion reactions. The experiments included $\gamma$-ray yields as a function of bombarding energy, $\gamma$-ray angular distributions, and three-detector $\gamma$-$\gamma$ coincidence measurements. The positive-parity band based on the unique-parity $g_{9/2}$ orbital in both nuclei exhibits a $\Delta I = 1$ character, unlike its counterpart $h_{11/2}$ band in Pd nuclei. The energy levels, $\gamma$-ray mixing ratios, branching ratios, and lifetimes in this band as well as in the ground-state negative-parity band are shown to be in good agreement with calculations using a particle-plus-rotor model at a small, symmetric deformation ($\delta = 0.12$). The Coriolis and recoil effects are explicitly included and a variable moment of inertia is used. The low-lying "anomalous" $7/2^+$ state is also readily reproduced by this model. The calculation also shows that the $\Delta I = 1$ nature of the positive-parity band results primarily from the fact that the Fermi surface is far from the $K = 1/2$ state, whereas the transition properties are governed by the Coriolis mixing of the strong-coupled bands. Two bands built on the $17/2^-$ and $21/2^+$ states with high bandhead energies are thought to have three-quasiparticle configurations.

NUCLEAR STRUCTURE $^{92}$Zr($^{16}$O,$p2n$) $^{105}$Ag at 60 MeV, $^{96}$Zr($^{14}$N, $3n$)$^{107}$Ag at 49 MeV: measured $I_\gamma(E(^{16}\mathrm{O}))$, $I_\gamma(E(^{14}\mathrm{N}))$, $I_\gamma(\theta)$, $\gamma$-$\gamma$ coin, $\gamma$-$\gamma$ DCOQ. $^{105,107}$Ag deduced levels, $J$, $\pi$, $\gamma$ mixing ratios. Rotational model calculations, Coriolis, calculated levels, mixing ratios, branching ratios, lifetimes. Ge(Li) detectors.

## I. INTRODUCTION

Nuclei in the mass-100 region ($Z \leq 50$, $N \geq 50$) provide an excellent opportunity to investigate rotational phenomena in transitional muclei. Previous investigations have shown that the states observed following (H.I.,$xn$) reactions in $^{101,103,105}$Pd (Refs. 1 and 2), $^{105,107,109}$Cd (Ref. 3), and $^{106,108}$Cd (Ref. 4) are in good agreement with a Coriolis coupling calculation using a slightly deformed, symmetric rotor with a variable moment of inertia. The Coriolis calculation used for Pd and Cd nuclei is the same as that used for strongly deformed nuclei,[5] except that the deformation is smaller and a variable moment of inertia is included. A variable moment of inertia does not necessarily represent a departure from the situation observed for strongly deformed nuclei where too the energies of high-spin rotational states fall below the prediction of a rigid rotor. The physical reasons for compression of rotational bands are not understood clearly. The mechanism may involve either a real change in the inertial properties of the nucleus, or an apparent change due to the mixing of zero-quasiparticle and multi-quasiparticle states. In either case the larger rotational energies and angular frequencies associated with small nuclear deformations could result in substantial compression of rotational bands at lower spins in slightly deformed nuclei.

In the slightly deformed rotor description, major systematic differences in the structure of collective bands can be understood by considering the position of the quasiparticle bandhead relative to the Fermi surface. Although the Coriolis term mixes states with different values of $\Omega$, it is useful to classify bands by the average value of $\Omega$. When the average $\Omega$ value is low, the Coriolis interaction drastically reduces the energy of aligned states that have $I = R + j$, where $R$ and $j$ are the angular momenta of the core and the odd particle, respectively, and $I$ is the total angular momentum of the nucleus. These aligned states usually are near the yrast line and are strongly populated while the nonaligned states (with $I \leq R + j - 1$) are above the yrast line and are populated weakly by heavy-ion reactions. Thus the primary characteristic of a low-$\Omega$ band is a cascade of $E2$ $\gamma$ rays between states that have $\Delta I = 2$. A low-$\Omega$ band is described as "decoupled" because the energy spacing of aligned states is similar to the spacing of the ground-state band in the neighboring even-even nucleus which corresponds to the core.

When the average $\Omega$ value is high, the Coriolis interaction does not reduce the energy of a selected set of states, and the collective band has a sequence of states with $\Delta I = 1$, similar to strongly deformed nuclei. In such a band, $\Delta I = 1$ mixed transitions compete with $\Delta I = 2$ transitions.

Many one-quasiparticle states in odd-neutron mass-100 nuclei have low $\Omega$ values because there are only a few neutrons outside the closed 50 shell. Therefore, decoupled bands built on one-quasiparticle states are a major feature of these nuclei. The odd-proton nuclei $^{105,107}$Ag, which are the subject of this paper, are particularly interesting because the $g_{9/2}$ orbital is nearly full (3 holes); hence there should be a low energy $\frac{9}{2}^+$ state with a relatively high $\Omega$. In the slightly deformed rotor description it is expected that these nuclei will have a $\Delta I = 1$ band built on a $\frac{9}{2}^+$ state. Since the Ag core is similar to that of Pd, the model parameters are constrained and it is not possible to force the model to fit the data. The predictions for Pd and Ag, however, are quite different. It is shown in this paper that the slightly deformed rotor description of Ag is in very good agreement with the experimental level scheme. This is a much more valid test of the model than could be obtained by interpreting nuclei with similar characteristics.

The coupled bands observed in odd-proton Ag nuclei also provide a convenient way to test details of the wave functions obtained from the Coriolis coupling calculation. $\gamma$-ray branching ratios and $E2$-$M1$ mixing ratios can be calculated for transitions in the coupled bands and compared to the experimental values.

## II. EXPERIMENTAL PROCEDURES

### A. General considerations

All measurements were performed following the fusion of incident heavy-ions with target nuclei. Several unobserved particles ($\alpha$, $p$, or $n$) were evaporated from the compound nucleus, and the subsequent cascades of $\gamma$ rays were observed with in-beam spectroscopy. The intensities of $\gamma$ rays were measured as a function of the incident projectile energy to aid in the assignment of $\gamma$ rays to specific nuclei. $\gamma$-$\gamma$ coincidence measurements were employed to determine the decay scheme of the nuclei. The coincidence data also were used with $\gamma$-ray angular distributions to obtain angular momentum changes of $\gamma$-ray transitions.

Most of the data were obtained with the reactions $^{96}$Zr($^{14}$N, $3n$)$^{107}$Ag at a beam energy of 49 MeV and $^{92}$Zr($^{16}$O, $p2n$)$^{105}$Ag at 60 MeV, although other reactions (to be described later) were also used to confirm the assignment of $\gamma$ rays to specific nuclei. Both targets were enriched; the $^{92}$Zr was essentially 100% pure whereas the $^{96}$Zr was 87% pure, the contaminants being 7% $^{90}$Zr, 2% $^{92}$Zr, and 4% $^{94}$Zr. The targets were rolled foils 2 mg/cm$^2$ thick with approximately 4 mg/cm$^2$ of gold evaporated on the back of each target to stop recoiling Ag nuclei and reduce the $\gamma$-ray Doppler shift. A 25 $\mu$m Au sheet was placed immediately behind the target to stop the beam. Beam currents of 10 to 20 nA were supplied by the Purdue FN tandem Van de Graaff accelerator.

The Ge(Li) detectors used in these measurements had active volumes of 25 to 45 cc and energy resolutions from 2.2 to 2.5 keV full width at half maximum (FWHM) at a $\gamma$-ray energy of 1333 keV. For singles measurements, a $^{60}$Co source was mounted on the detector so that the 1173.26- and 1332.59-keV $\gamma$ rays from it could be counted simultaneously with $\gamma$ rays from the target. Since the 191.48-, 278.92-, and 547.55-keV $\gamma$ rays from Coulomb excitation of the Au backing were always present, five internal reference lines of well-known energies were available in each spectrum. The nonlinearity of the detector-electronics system was measured using $^{182}$Ta and $^{152}$Eu sources. The $\gamma$-ray energies reported in this paper are typically accurate to ±50 eV.

Excitation functions for each reaction were run over a range of 12 MeV to select the best incident energy for the measurements. (The average energy in the target was typically 3 MeV lower than the incident energy.) The energy was set on the high side of the maximum yield for $\gamma$ rays from low energy states, in order to increase the yield from high angular momentum states. This choice also increased the $\gamma$-ray yield from the reactions $^{96}$Zr($^{14}$N, $4n$)$^{106}$Ag and $^{92}$Zr($^{16}$O, $3n$)$^{105}$Cd. The results for $^{106}$Ag and $^{105}$Cd will be reported in subsequent publications (Refs. 6 and 3, respectively).

A large number of nuclei were produced in the $^{14}$N bombardment of the $^{96}$Zr target corresponding to the various isotopic impurities in the target and the multiplicity of exit channels (relative production is indicated in parentheses): $^{106}$Ag from $4n$(300), $^{107}$Ag from $3n$(100), $^{106}$Pd from $p3n$(60), $^{107}$Pd from $p2n$(8), $^{105}$Ag from $^{94}$Zr-$3n$(11), $^{104}$Ag from $^{94}$Zr-$4n$(3), $^{102}$Pd from $^{90}$Zr-$pn$(6), $^{101}$Pd from $^{90}$Zr-$p2n$(14), $^{104}$Pd from $^{94}$Zr-$p3n$(6), $^{103}$Rh from $^{94}$Zr-$\alpha n$(3), $^{101}$Rh from $\beta^+$ decay of $^{101}$Pd(6), and $^{96}$Zr from Coulomb excitation (47). The following nuclei were observed from the $^{16}$O bombardment of $^{92}$Zr: $^{105}$Cd from $3n$(220), $^{105}$Ag from $p2n$(100), $^{106}$Cd from $2n$(30), $^{104}$Pd from $\alpha$(17), $^{102}$Pd from $\alpha 2n$(34), $^{103}$Pd from $\alpha n$(4), $^{104}$Ag from $p3n$(6), $^{104}$Cd from $4n$(16), and $^{92}$Zr from Coulomb excitation (45).

### B. Identification of $^{107}$Ag and $^{105}$Ag

When $\gamma$ rays from such a large number of nuclei are observed together, a great deal of care must be taken in assigning transitions to a specific nucleus. If transitions between low energy states are known, many other transitions which feed these states can be assigned with the help of coincidence data. However, most $\gamma$ rays from these Ag nuclei were not in coincidence with known $\gamma$ rays; therefore, the most reliable procedure for assigning transitions to particular nuclei was to compare the intensity of $\gamma$ rays from measurements following various heavy-ion reactions.

The coincidence data from the $^{14}$N reaction revealed three strongly populated $\gamma$-ray cascades. One of these, with 511.78- and 717.31-keV $\gamma$ rays at the bottom, was well known from the previous investigation of $^{106}$Pd (Ref. 7). The other two cascades were characterized by strong 865–1063-keV and 170-676-377-keV coincidences. Since the compound nucleus formed by the fusion of $^{14}$N and $^{96}$Zr has $Z=47$, the only nuclei formed in the reaction would be isotopes of Ag ($Z=47$), Pd ($Z=46$) and Rh ($Z=45$) corresponding to the outgoing particles ($xn$), ($pxn$), and ($\alpha xn$), respectively. The 865- and 170-keV coincidences were also observed in heavy-ion reactions that formed a Cd compound nucleus ($Z=48$); therefore, they could not be associated with Rh ($Z=45$). Pd isotopes also were eliminated since the decay schemes of $^{104-108}$Pd are well known[1,7-9] and do not match our data. Therefore, the two cascades must come from Ag isotopes.

The variation in yields of $\gamma$ rays with beam energy from the $^{14}$N excitation functions showed that the number of neutrons emitted in the production of $\gamma$ rays in coincidence with the 865-keV $\gamma$ ray and the 170-keV $\gamma$ ray were most likely 3 and 4, respectively. Since the compound nucleus $^{110}$Ag was formed in the bombardment of $^{96}$Zr by $^{14}$N, the cascades feeding the 865-keV transition and the 170-keV transition would be in $^{107}$Ag and $^{106}$Ag, respectively. These assignments were confirmed by comparing the intensities of these cascades from reactions that would have very different probabilities of producing $^{106}$Ag and $^{107}$Ag. When $^{94}$Zr was bombarded with 59-MeV $^{16}$O, ($p2n$) production of $^{107}$Ag was more probable than ($p3n$) production of $^{106}$Ag. The cascade in coincidence with the 865-keV $\gamma$ ray was seen to be much more intense than that in coincidence with the 170-keV $\gamma$ ray in this reaction. The relative intensities were reversed when $^{97}$Mo was bombarded with 45-MeV $^{12}$C producing $^{106}$Ag by ($p2n$) and $^{107}$Ag by ($pn$).

$^{105}$Ag has been studied by Svensson *et al.*[10] using a ($p,n$) reaction which produces a much smaller number of isotopes than the heavy-ion reaction used here. The 864- and 616-keV $\gamma$ rays observed in our $^{16}$O experiment are no doubt the same as the $\frac{13}{2}\rightarrow\frac{9}{2}$ and $\frac{11}{2}\rightarrow\frac{9}{2}$ transitions of the same energies reported in Ref. 10. These assignments were confirmed by data similar to that used for $^{107}$Ag and by the similarity between the decay schemes of $^{107}$Ag and $^{105}$Ag.

### C. $\gamma$-$\gamma$ coincidence measurements

Considering the number of isotopes formed in each of these heavy-ion reactions, it is expected that the $\gamma$-ray spectra will be very complex. A singles spectrum from the $^{14}$N reaction is shown in Fig. 1 as an example. Many peaks in the $\gamma$-ray singles spectra represent more than one transition; therefore, good statistical accuracy and precise data treatment in $\gamma$-$\gamma$ coincidence measurements must be emphasized. Since our $\gamma$-$\gamma$ coincidence technique has been described previously,[7] only a summary will be given here.

Three Ge(Li) detectors were used to give a three-fold improvement in the coincidence data rate (typically 2000 to 4000 events per second) over a two-detector system. For each reaction, approximately $10^8$ coincidence events were recorded, and approximately 300 gates were set on $\gamma$-peaks and Compton backgrounds. Each gate generated three coincidence spectra, one for each pair of detectors. This obviously presented a massive data handling problem, but it was essential to obtain reliable information on important weak transitions. The data were recorded event by event on magnetic tape and sorted after the measurement to construct the coincidence spectra using a PDP-15 computer. Corrections were made for accidental coincidences, detector efficiency, fractions of peaks covered by gates, and coincidence circuit efficiency. The three detectors were positioned at angles of 0°, 100°, and −100° with respect to the beam line so that $\gamma$-ray intensities could be determined from the coincidence data. With this combination of angles, the average of the six coincidence areas associated with the three pairs of detectors is proportional to the true coincidence intensity to within 5%, independent of the multipolarity of the $\gamma$ ray. This choice of angles also gives good sensitivity for the DCO analysis described below. With the high data rate and these precautions, the coincidence measurements provided $\gamma$-ray intensity and energy values which have similar accuracy to that usually obtained from singles measurements.

The detectors were located approximately 2.5 cm from the target. Compton scattering of $\gamma$ rays from one detector into another was reduced by placing lead absorbers inside and outside of the target chamber. The time pickoffs from the three detectors were connected through a multiplexer to one time-to-amplitude converter. Two single-channel

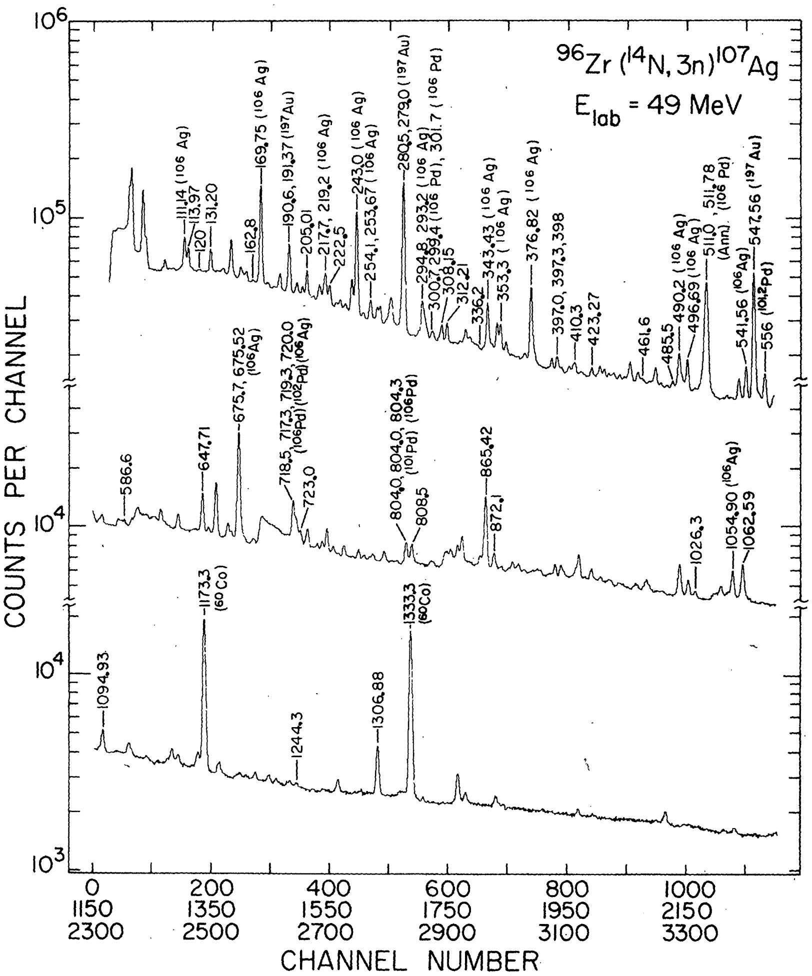

FIG. 1. Singles spectrum from the $^{96}$Zr($^{14}$N, $3n$) $^{107}$Ag reaction.

analyzer gates were set on the output of the time-to-amplitude converter so that the coincidence events could be identified as either true-plus-chance or chance.

The digital gates were set on spectra showing all the $\gamma$ rays in one detector in coincidence with any $\gamma$ ray in the other two detectors. Sample gated spectra are shown in Fig. 2. These gates do not represent the strongest lines in the spectra but are typical and do indicate the average quality of the coincidence data.

### D. DCOQ analysis of coincidence data

The directional correlation from orientated nuclei (DCO) technique[11] was used to determine angular momentum changes and mixing ratios for transitions unresolved in the singles spectra. The basic information unit was the ratio of the two coincidence intensities $N_{12}$ and $N_{21}$, where $N_{12}$ was the number of times $\gamma_1$ was detected in detector $x$ with $\gamma_2$ in detector $y$:

$$R_{\text{DCO}} = \frac{N_{12}}{N_{21}}.$$

This ratio can be calculated for various multipolarities and mixing ratios for both $\gamma_1$ and $\gamma_2$. The ideal case is that where $\gamma_2$ is a quadrupole transition, since the ratio is easily interpreted. Theoretically, all ratios involving the same $\gamma_1$ in coincidence with different quadrupole transitions $\gamma_2$ are equal, so that several such ratios can be combined for better statistical accuracy. If $\gamma_2$ is not a quadrupole, a corrected ratio can be calculated if the ratio involving $\gamma_2$ and a known quadrupole transition $\gamma_3$ has also been measured. Thus, a large number of DCO ratios can be suitably combined to construct an average ratio for $\gamma_1$ compared to quadrupole transitions, called an average DCOQ ratio. Details of this procedure are described in Ref. 7.

In the DCOQ analysis the experimental values are compared to a detailed calculation of the DCOQ ratio. However, there are several gen-

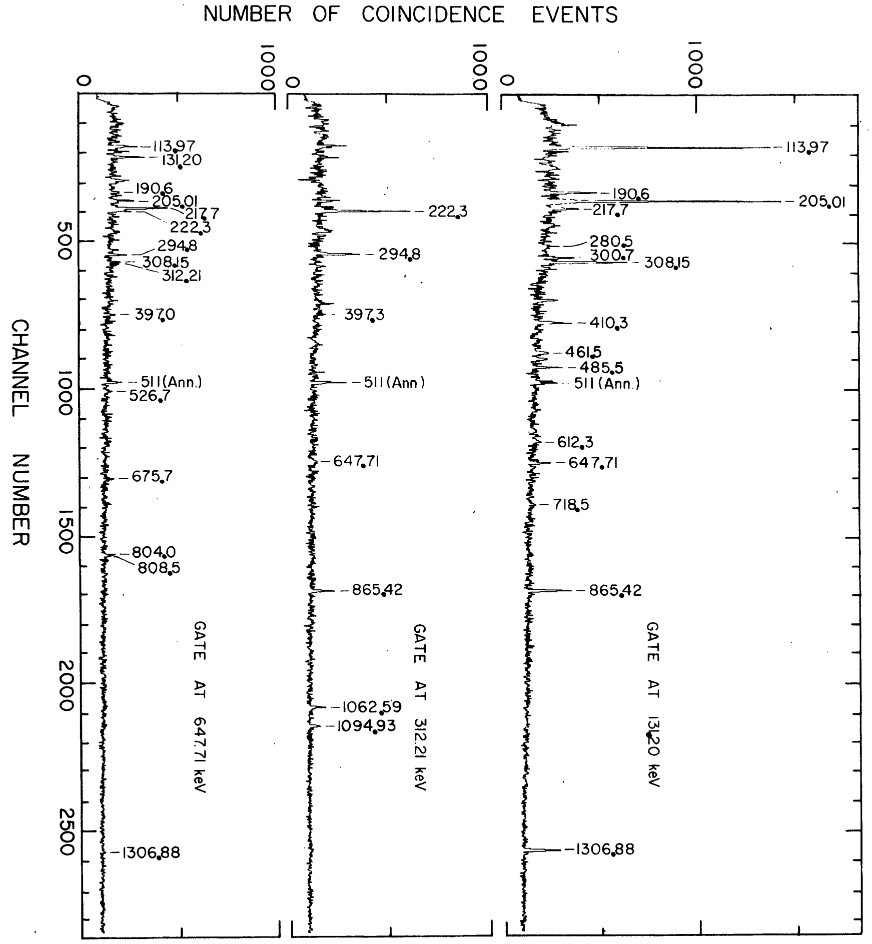

FIG. 2. Sample gated coincidence spectra from the $^{96}$Zr($^{14}$N, $3n$)$^{107}$Ag reaction. Chance events and ADC-A Compton events have been subtracted.

eral guidelines for a simplified interpretation of average DCOQ ratios. The DCOQ ratio is approximately equal to the ratio of the anisotropies of the two transitions. Thus, (1)$R_{\mathrm{DCOQ}} = 1$ is characteristic (but not uniquely) of a $\Delta I = -2$ transition, (2)$R_{\mathrm{DCOQ}} \simeq 2$ implies a $\Delta I = \pm 1$ pure-dipole transition, (3)$R_{\mathrm{DCOQ}} > 3$ uniquely describes a mixed $\Delta I = \pm 1$ transition, and (4)$R_{\mathrm{DCOQ}} < 1$ implies $\Delta I = 0$ or $\Delta I = \pm 1$.

### E. Angular distributions

When a $\gamma$ ray is resolved in the singles spectra, better accuracy can be obtained using an angular distribution rather than DCOQ analysis. Precise angular distributions were necessary to determine mixing ratios which could be compared to values obtained with wave functions from the Coriolis coupling calculation. The angular distribution measurements were made at nine evenly spaced angles from +90° to −30° with respect to the beam axis. Other details of procedures used in the angular distribution measurements have been described previously.[12,13]

The experimental angular distributions were fitted to the usual function

$$W(\theta) = A_0 Q_0 \left[ 1 + A_{22}\frac{Q_2}{Q_0} P_2(\cos\theta) + A_{44}\frac{Q_4}{Q_0} P_4(\cos\theta) \right],$$

where the $Q_k$ are solid angle correction factors, and $A_0$ is a measure of the total $\gamma$-ray intensity. The analysis of angular distribution (and DCOQ) measurements is complicated by the nuclear deorientation that occurs when particles or unobserved $\gamma$ rays are emitted. As shown previously[12,13] this problem can be handled with a systematic analysis of related transitions. The effect of deorientation is included in the distribution coefficients by the parameters $\alpha_k$ defined by

$$A_{kk} = \alpha_k A_{kk}^0 .$$

The $A_{kk}^0$ values can be calculated from the data tabulated by Yamazaki.[14] For pure multipole transitions, the calculated $A_{kk}^0$ and the experimentally measured $A_{kk}$ can be used to determine the deorientation coefficient $\alpha_k$. The $\alpha_k$ values for mixed transitions can then be calculated from those of neighboring pure transitions, taking into account any deorientation due to $\gamma$-ray emission.[12,13]

Angular distribution and DCOQ measurements can be used to determine the change in angular momentum ($\Delta I$) associated with a transition, but they are both insensitive to whether $I$ increases or decreases. However, for transitions observed following heavy-ion reactions, this ambiguity can be removed in many cases by using an yrast argument, i.e., at a given energy, the state with highest angular momentum is preferentially populated. Thus when a transition is observed from a state with $I_i$ to a state with $I_f$, it is much more likely that $I_i = I_f + \Delta I$ than $I_i = I_f - \Delta I$. This yrast argument is stronger for $\Delta I = 2$ transitions than for $\Delta I = 1$ transitions, but additional consistency arguments, which will be illustrated in the discussion of the decay schemes, usually remove the ambiguity in angular momentum assignments.

Likely parity assignments can also be made from angular distribution and DCOQ measurements. Highly mixed $E1$-$M2$ transitions are very improbable; therefore, a substantial mixing ratio for a $\Delta I = 1$ or $\Delta I = 0$ transition strongly indicates that there is a $E2$-$M1$ mixture and parity is not changed.

## III. EXPERIMENTAL RESULTS

### A. Decay scheme for $^{107}$Ag

A 423-keV transition to the $\frac{1}{2}^-$ ground state of $^{107}$Ag was known[15] beforehand, and the 865-keV $\gamma$ ray was assigned in this investigation as already described. All other $\gamma$ rays were assigned to $^{107}$Ag on the basis of coincidences with these $\gamma$ rays. The construction of the decay scheme required not only yes or no coincidence information but also a consistent interpretation of singles and coincidence intensities. Precise $\gamma$- ray energies were used to confirm placements, but no $\gamma$ rays were placed solely on the basis of energies.

The analysis for 38 $\gamma$ rays assigned to $^{107}$Ag is summarized in Table I. Column 1 lists precise $\gamma$-ray energies, determined from singles spectra for well-resolved $\gamma$ rays and from gated coincidence spectra otherwise. Total transition intensities including corrections for internal conversion[16] are listed in column 2. When the singles and coincidence intensities agreed, the singles intensity was adopted. A singles intensity significantly larger than the coincidence intensity was taken as an indication of unresolved $\gamma$ rays in the singles spectra, and the coincidence intensity was adopted. In most cases the source of the $\gamma$-ray interference was identified. Footnotes are used in column 2 for the source of intensity information and to indicate the extent of the interference.

The angular distribution coefficients, corrected for detector solid angle, are listed in columns 3 and 4. The deorientation coefficients listed in columns 5 and 6 were determined from the angular distributions of $E2$ transitions and used in the calculation of mixing ratios. DCOQ ratios for heavily contaminated transitions are listed in column 7. Footnotes are used in column 8 to indicate the origin of data used to calculate mixing ratios.

The level scheme for $^{107}$Ag is presented in Fig. 3. Four $\gamma$ rays indicated by dashed arrows are placed tentatively. Intensities are shown in parentheses, and the solid arrows represent $E2$ transitions.

The yrast argument discussed in Sec. II has been used to assign spins for states depopulated by $\Delta I = 2$ transitions. The following systematic argument has also been used to remove ambiguities in the spins of states decaying by $\Delta I = 1$ transitions: A set of states which looks like a regular collective band is likely to have monotonically increasing spins. The "reversal" of spin order implied by a $\Delta I = +1$ transition would probably cause the corresponding state to be depopulated by several $\Delta I = 0$, 1, and 2 transitions feeding lower levels. For example, if the 308-keV $\gamma$ ray depopulating the 3056.3-keV state were to have $\Delta I = +1$, i.e., if this state had $I = \frac{19}{2}$, then it could decay not only to the $\frac{21}{2}$ and $\frac{19}{2}$ states below, but also to the $\frac{17}{2}$ and $\frac{15}{2}$ states; in fact, the energy factor would favor the latter transitions. The absence of these transitions and the yrast argument make a $\Delta I = +1$ assignment most unlikely.

The parity of the $\frac{15}{2}$ state at 2298.0 keV cannot be determined definitely from our measurements. However, since the mixing ratio of the 1307-keV $\gamma$ ray is nearly zero and the mixing ratios for $M1$-$E2$ transitions increase with energy, it is very probable that this is an $E1$ $\gamma$ ray. In that case, the $\frac{15}{2}$ state would have negative parity. This result also follows from analogy with the $\frac{15}{2}^-$ state in $^{105}$Ag, described in the next subsection. The higher energy states ($\frac{17}{2}$, $\frac{19}{2}$, etc.) also have negative parity since the $\Delta I = 1$ connecting transitions are definitely mixed. A few other assignments require additional discussion.

*423.3-keV state.* Table I shows that the angular distribution of the 423.3-keV $\gamma$ ray is not appropri-

TABLE I. Analysis for $\gamma$ rays emitted following the $^{96}$Zr($^{14}$N,3$n$)$^{107}$Ag reaction at 49 MeV.

| Energy (keV) | Relative intensity | $A_{22}$ | $A_{44}$ | $\alpha_1$ | $\alpha_2$ | $R_{\mathrm{DCOQ}}$ | $\delta$ |
|---|---|---|---|---|---|---|---|
| 113.97(7) | 36 (1)[b] | −0.145(12) | −0.044(14) | 0.83(7) | 0.54(13) | 1.76(7) | 0.05(2)[e] |
| 120 (1) | 1.2(3)[c] | | | | | | |
| 131.20(5) | 33.6(3)[a] | −0.126(15) | −0.028(19) | 0.85(8) | 0.58(18) | | 0.08(2)[d] |
| 162.8 (7) | 0.9(2)[a] | | | | | | |
| 190.6 (2) | 4.4(4)[c] | | | | | 1.66(30) | 0.08(7)[e] |
| 205.01(6) | 25.1(5)[b] | −0.080(14) | −0.013(17) | 0.87(9) | 0.64(20) | 1.57(7) | 0.09(2)[e] |
| 217.7 (2) | 15.5(3)[a] | −0.065(39) | −0.051(49) | 0.66(3) | 0.27(6) | | 0.10(5)[d] |
| 222.5 (1) | 15.3(7)[b] | −0.087(19) | −0.008(28) | 0.86(7) | 0.60(18) | 1.60(13) | 0.12(4)[e] |
| 254.1 (5) | 2 (1)[c] | | | | | | |
| 280.5 (5) | 1.8(3)[c] | | | | | | |
| 294.8 (1) | 12 (1)[c] | | | | | 1.89(20) | 0.06(4)[e] |
| 300.7 (2) | 2.9(7)[b] | | | | | 1.52(26) | 0.12(7)[e] |
| 308.15(8) | 18.2(2)[a] | −0.045(21) | −0.014(27) | 0.88(10) | 0.67(22) | | 0.12(2)[d] |
| 312.21(7) | 16 (1)[b] | −0.208(25) | −0.004(32) | 0.84(6) | 0.56(16) | 1.42(12) | 0.17(4)[e] |
| 336.2 (4) | 2.2(8)[b] | | | | | | |
| 397.0 (3)[f] | 5.4(9)[c] | | | | | | |
| 397.3 (2)[g] | 4 (2)[c] | | | | | 1.85(46) | 0.08(9)[e] |
| 398 (1)[h] | 2.9(7)[c] | | | | | | |
| 410.3 (2) | 10.7(3)[a] | −0.036(51) | −0.064(64) | 0.89(10) | 0.69(22) | | 0.13(3)[d] |
| 423.27(6) | 8.7(2)[a] | 0.127(50) | −0.064(75) | 0.57(11) | 0.25(25) | 0.74(24) | $E2$[i] |
| 461.6 (2) | 5.4(3)[a] | | | | | | |
| 485.5 (2) | 6.5(2)[a] | −0.17(7) | 0.00(10) | 0.87(9) | 0.64(26) | 1.94(38) | 0.05(5)[d] |
| 514 (1) | 0.9(4)[b] | | | | | | |
| 526.7 (1) | 4 (1)[a] | −0.8(2) | 0.62(26) | 0.80(10) | 0.50(20) | | 0.25(5)[d] |
| 586.6 (5) | 6.3(3)[a] | −0.54(8) | 0.22(11) | 0.75(15) | 0.39(23) | | −3.0(9)[d] |
| 612.3 (5) | 4.2(7)[b] | | | | | | |
| 647.71(5) | 47.9(5)[a] | 0.173(18) | 0.056(23) | 0.59(7) | 0.22(7) | | 0.33(8)[d] |
| 675.7 (2) | 9 (2)[c] | | | | | 0.54(34) | |
| 718.5 (5) | 2.3(6)[c] | | | | | | |
| 723.0 (2) | 9 (1)[b] | 0.33(5) | −0.14(7) | 0.68(10) | 0.49(23) | | $E2$[d] |
| 804.0 (2) | 14.6(3)[b] | 0.22(4) | 0.03(5) | 0.75(15) | 0.39(23) | 1.1(3) | $E2$[e] |
| 808.5 (2) | 18 (2)[a] | 0.17(7) | 0.06(9) | 0.79(6) | 0.48(10) | 1.36(37) | 0.27(8)[d] |
| 865.42(5) | 100.0(0)[a] | 0.289(12) | −0.043(14) | 0.66(3) | 0.20(6) | | $E2$[d] |
| 872.1 (5) | 3.3(7)[c] | | | | | | |
| 1026.3 (2) | 3 (1)[b] | 0.20(13) | 0.03(17) | 0.79(16) | 0.48(10) | | $E2$[d] |
| 1062.6 (1) | 34.1(4)[a] | 0.34(3) | −0.027(36) | 0.81(6) | 0.60(12) | | $E2$[d] |
| 1094.9 (1) | 19.4(5)[a] | 0.344(57) | −0.11(8) | 0.84(14) | 0.66(48) | | $E2$[d] |
| 1244.3 (2) | 4 (1)[b] | | | | | | |
| 1306.9 (1) | 42.5(4)[a] | −0.267(20) | 0.035(26) | 0.80(7) | 0.59(15) | | −0.01(2)[d] |

[a] Singles and coincidence intensity agree. Singles intensity adopted.

[b] Coincidence intensity adopted. Interference in singles from a $\gamma$ ray of similar intensity.

[c] Coincidence intensity adopted. Interference in singles from a $\gamma$ ray of greater intensity.

[d] Angular distribution used to determine mixing ratio.

[e] DCOQ used to determine mixing ratio.

[f] $\gamma$ ray depopulates the 1846.0-keV level.

[g] $\gamma$ ray depopulates the 4375.5-keV level.

[h] $\gamma$ ray depopulates the 4773-keV level.

[i] Assignment discussed in text.

ate for a $\Delta I=2$ transition. We suspect that there is an error in the $A_{22}$ of this $\gamma$ ray because of uneven background. Other workers[15] have firmly identified this state as $I^{\pi}=\frac{5}{2}^{-}$. Our DCOQ value is consistent with this assignment.

*773.4-keV state*. This is an example of a common situation where the $\Delta I=+1$ possibility for a $\gamma$ ray can be definitely ruled out. The $I$ of the 991.1-keV level is firmly established as $\frac{13}{2}$ because the 865.42-keV $\gamma$ ray has $\Delta I=-2$. Since both the 217.71- and 647.71-keV $\gamma$ rays are known to have $\Delta I=1$, they both must cause a decrease in $I$. Hence $I=\frac{11}{2}$ is established for the 773.4-keV state.

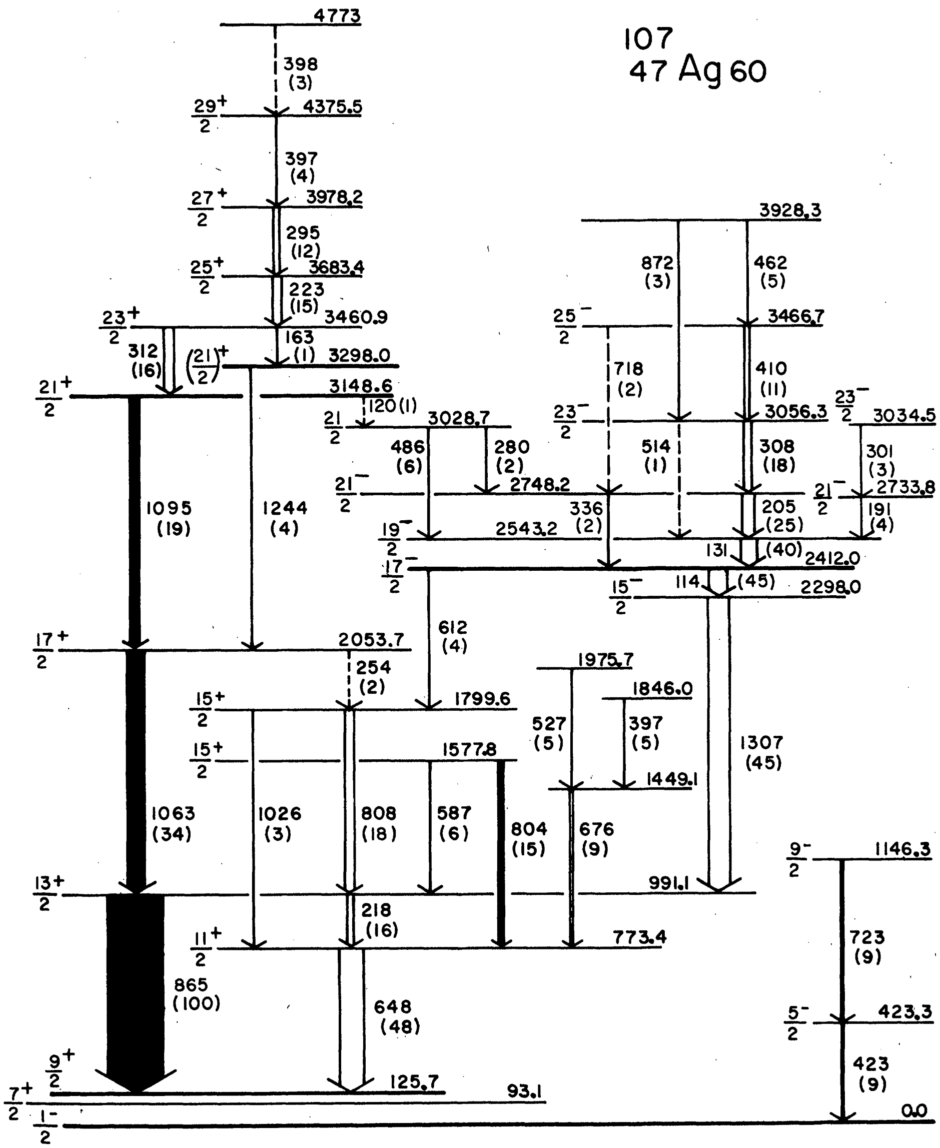

FIG. 3. Decay scheme for $^{107}$Ag. Solid arrows indicate $E2$ transitions. The numbers in parentheses are relative transition intensities, including internal conversion.

*1449.1- and 1975.7-keV states.* The 675.7-keV transition has $R_{\mathrm{DCOQ}} = 0.54(34)$. (The angular distribution is of no help because the $\gamma$ ray is masked by the much stronger $\gamma$ ray from $^{106}$Ag.) The large error makes the spin-parity of the 1449.1-keV level very uncertain. Only $\frac{13}{2}^-$ can be ruled out. The 526.7-keV $\gamma$ ray has $\Delta I = 1$ and does not change parity. Thus, if the 1449.1-keV level had spin-parity $\frac{13}{2}^+$, the 1975.7-keV level would have $\frac{15}{2}^+$.

### B. Decay scheme for $^{105}$Ag

Until recently, the only results available on $^{105}$Ag structure were on low-spin states. During the course of this investigation, however, two reports on $^{105}$Ag populated by $^{103}$Rh$(\alpha, 2n)$ reaction have been published by Hippe *et al.*[17] and Kalshoven *et al.*[18] Our results generally agree with and, in some respects, add to theirs.

Table II presents the results of the analysis for 38 $\gamma$ rays assigned to $^{105}$Ag. It is apparent from the table that there is substantial interference between many $\gamma$ rays in the singles spectra. The $^{105}$Ag decay scheme is presented in Fig. 4. A cascade similar to that feeding the $\frac{21}{2}^+$ state in $^{107}$Ag is not shown, although there is some evidence for such a structure in $^{105}$Ag. A cascade of three $\gamma$ rays with energies of 169,

TABLE II. Analysis for $\gamma$ rays emitted following the $^{92}$Zr($^{16}$O,$p2n$)$^{105}$Ag reaction at 60 MeV.

| Energy (keV) | Relative intensity | $A_{22}$ | $A_{44}$ | $\alpha_2$ | $\alpha_4$ | $R_{\mathrm{DCOQ}}$ | $\delta$ |
|---|---|---|---|---|---|---|---|
| 98.91(11) | 11 (2)[c] | | | | | 3.6(5) | −0.12(5)[e] |
| 126.05(15) | 8 (1)[c] | | | | | 3.5(5) | −0.12(5)[e] |
| 155.42(6) | 47.1(5)[a] | −0.184(10) | 0.017(13) | 0.82(3) | 0.53(5) | | 0.04(1)[d] |
| 184.54(7) | 45.3(6)[a] | −0.146(11) | 0.012(15) | 0.83(3) | 0.55(5) | | 0.06(1)[d] |
| 240.29(8) | 37.1(6)[a] | −0.175(15) | 0.018(19) | 0.84(2) | 0.57(5) | | 0.05(1)[d] |
| 248.65(7) | 30 (1)[b] | −0.165(14) | 0.009(18) | 0.74(3) | 0.38(5) | 2.13(22) | 0.00(4)[e] |
| 290.40(15) | 5 (1)[c] | | | | | | |
| 296.50(15)[f] | 5 (1)[b] | | | | | 0.92(16) | 0.22(38)[e] |
| 297.04(30)[f] | 4 (1)[b] | −0.094(53)[g] | 0.017(70)[g] | 0.77(8) | 0.43(14) | | 0.09(4)[d] |
| 334.51(10) | 34.5(6)[a] | −0.105(14) | −0.009(19) | 0.85(2) | 0.59(5) | | 0.085(10)[d] |
| 339.96(13) | 2.0(7)[c] | | | | | | |
| 341.47(30) | 4.9(10)[b] | −0.074(65)[h] | 0.029(27)[h] | 0.73(11) | 0.37(14) | | 0.09(5)[d] |
| 346.77(40) | 8 (2)[c] | | | | | | |
| 417.27(8) | 24 (1)[a] | −0.157(35) | 0.068(54) | 0.86(2) | 0.60(5) | | 0.06(2)[d] |
| 424.83(15) | 3.4(8)[c] | | | | | | |
| 433.26(20)[f] | 8 (2)[c] | | | | | 1.77(60) | $E2$[e] |
| 433.91(18)[f] | 15 (2)[b] | | | | | 1.99(23) | 0.08(4)[e] |
| 448.55(12) | 8.5(8)[a] | 0.171(46) | −0.005(68) | 0.87(5) | 0.63(10) | | 0.26(4)[d] |
| 564.79(10) | 17 (1)[a] | −0.338(51) | 0.048(74) | 0.79(3) | 0.47(5) | | −0.07(5)[d] |
| 570.00(10) | 11 (1)[a] | | | | | | |
| 574.80(18) | 3 (1)[b] | | | | | | |
| 579.19(9) | 12.4(9)[a] | 0.371(64) | −0.031(93) | 0.89(11) | 0.18(53) | | $E2$[d] |
| 615.52(8) | 78 (1)[a] | 0.241(25) | 0.041(31) | 0.68(4) | 0.30(5) | | 0.35(4)[d] |
| 733.01(8) | 5.7(9)[a] | 0.30(13) | 0.00(20) | 0.62(28) | | | $E2$[d] |
| 751 (1) | 3.4(8)[b] | | | | | | |
| 763.78(8) | 23 (1)[a] | 0.149(37) | 0.090(58) | 0.79(10) | 0.45(17) | | 0.25(4)[d] |
| 816.63(25) | 12 (3)[a] | −1.112(93) | 0.26(14) | 0.70(5) | 0.30(5) | | −1.0(2)[d] |
| 851.18(26) | 3 (1)[c] | | | | | | |
| 864.14(9) | 100 | 0.325(12) | −0.097(17) | 0.74(3) | 0.45(8) | | $E2$[d] |
| 914.88(11) | 6 (1)[b] | | | | | | |
| 947.83(20) | 6 (1)[a] | | | | | | |
| 1012.43(25) | 9.8(8)[a] | 0.423(67) | −0.02(10) | 0.9(1) | 0.3(3) | | $E2$[d] |
| 1060.74(9) | 31 (1)[a] | 0.322(32) | −0.15(5) | 0.77(8) | 0.83(25) | | $E2$[d] |
| 1065.28(20) | 27 (2)[b] | 0.299(23) | −0.037(32) | 0.70(5) | 0.19(16) | | $E2$[d] |
| 1105.25(8) | 15.3(9)[a] | 0.306(45) | −0.066(66) | 0.73(11) | 0.36(36) | | $E2$[d] |
| 1147.09(12) | 8 (1)[a] | 0.42(17) | −0.30(24) | 1.8(2) | 0.6(3) | | $E2$[d] |
| 1552.39(12) | 12 (3)[b] | | | | | 1.84(34) | 0.07(7)[e] |
| 1579.50(12) | 21 (3)[b] | | | | | 1.99(20) | 0.05(5)[e] |

[a] Singles and coincidence intensity agree. Singles intensity adopted.

[b] Coincidence intensity adopted. Interference in singles from a $\gamma$ ray of similar intensity.

[c] Coincidence intensity adopted. Interference in singles from a $\gamma$ ray of greater intensity.

[d] Angular distribution used to determine mixing ratio.

[e] DCOQ used to determine mixing ratio.

[f] These transitions are unresolved in the singles spectra. They can be identified in the decay scheme by their intensity.

[g] Corrected for interference from the 296.5-keV transition. Uncorrected values are $A_{22} = 0.17(4)$ and $A_{44} = -0.01(5)$.

[h] Corrected for interference from the 339.96-keV transition. Uncorrected values are $A_{22} = 0.022(59)$ and $A_{44} = 0.00(9)$.

233, and 305 keV has been observed, but the data do not show these $\gamma$ rays in coincidence with the 1147-keV $\gamma$ ray depopulating the $\frac{21}{2}^+$ state in $^{105}$Ag. They seem to be feeding the $\frac{15}{2}^+$ state at 1681.2 keV through another $\gamma$ ray of energy 1094 keV.

Table II also shows the results of the angular distribution and DCOQ analyses. The DCOQ method proved to be of critical importance here, because there is extensive $\gamma$ ray interference in the singles. For example, the closely related group of $\gamma$ rays with energies 99, 126, 297, 1553, and 1580 keV are all contaminated. But the DCOQ analysis gives good results for their angular momentum changes.

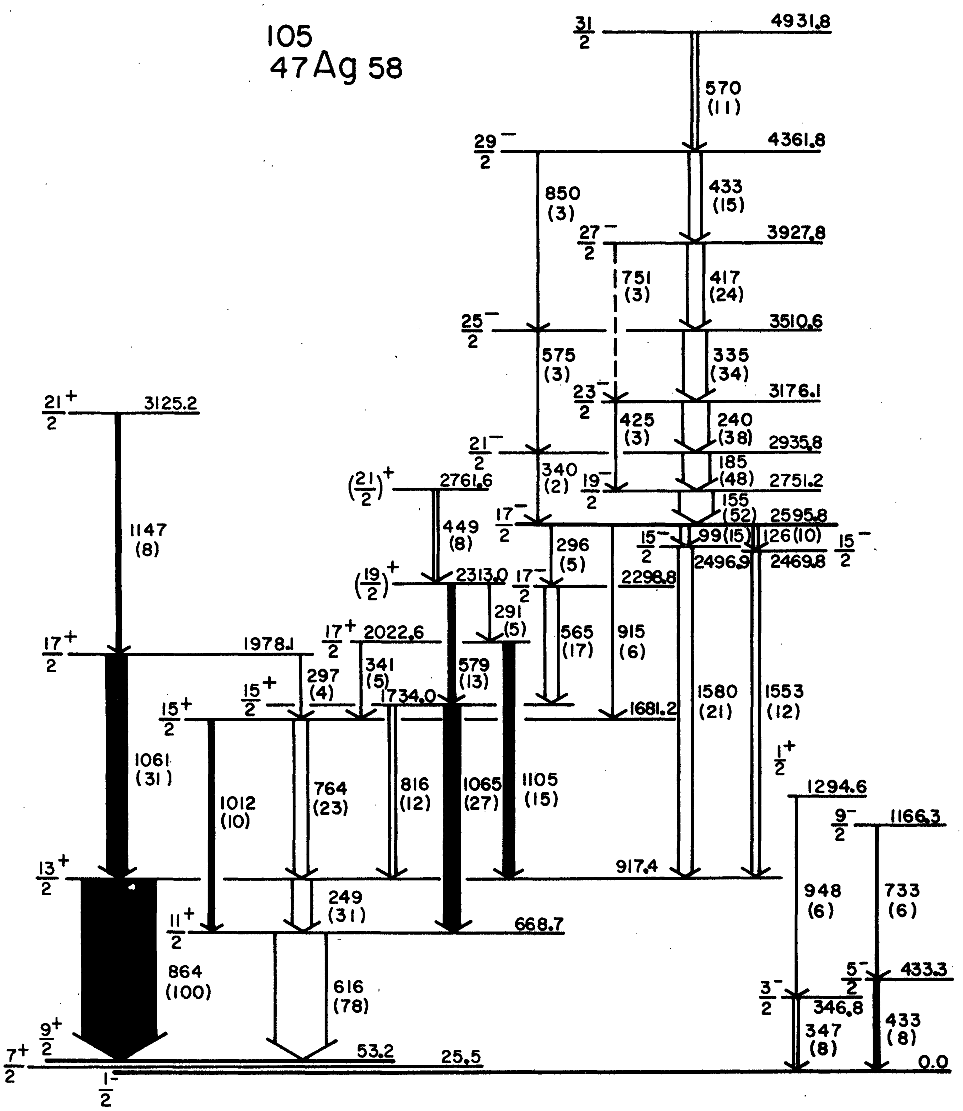

FIG. 4. Decay scheme for $^{105}$Ag. Solid arrows indicate $E2$ transitions. The numbers in parentheses are relative transition intensities, including internal conversion.

The parities of the two $\frac{15}{2}$ states at 2496.9 and 2469.8 keV and the $\frac{17}{2}$ state at 2298.8 keV are not determined in our angular distribution and DCOQ analyses. However, the $\gamma$-ray linear polarization and electron conversion data of Kalshoven *et al.* establish the parities of all three states as negative. The higher energy states which feed these two $\frac{15}{2}$ states have the same parity since the connecting transitions are definitely mixed. A few other assignments, which may not be obvious from the tables, are discussed below.

*433.3-keV state.* The ground-state transition gives a misleading angular distribution because a large part of the feeding of the 433.3-keV state is from $\beta^+$ decay of $^{105}$Cd. However, this transition is already known[10] to have $\Delta I = 2$. Hence the 433.3-keV level has $I^\pi = \frac{5}{2}^-$.

*668.7-keV state.* Like its counterpart in $^{107}$Ag, the spin-parity of this level is completely confirmed by the $\Delta I = 1$ character of the 616-keV and 248-keV $\gamma$ rays, and the $\Delta I = 2$ character of the 864-keV $\gamma$ ray.

*1294.6-keV state.* The angular distribution of the 948-keV $\gamma$ ray is completely distorted, probably because the 1294.6-keV state is populated by $\beta^+$ decay. Therefore the angular distribution does not give any information. However, from the $(p,n)$ and Coulomb excitation work of other investigators,[10] the 1294.6-keV state is known to have $I^\pi = \frac{1}{2}^+$.

Kalshoven *et al.*[18] have placed the members of the cascade of $\Delta I = 1$ $\gamma$ rays feeding the $\frac{17}{2}^-$ state at 2595.8 keV solely on the basis of intensities. Our observation of the $\Delta I = 2$ transitions in this band removes any ambiguity from this part of the decay scheme.

### C. Summary of level schemes

The level schemes of $^{107}$Ag and $^{105}$Ag, as described above, are quite similar. The ground state has spin-parity $\frac{1}{2}^-$, and there are low-lying $\frac{7}{2}^+$ and $\frac{9}{2}^+$ states. Although the $\frac{7}{2}^+$ state observed in Ag, Rh, and Tc nuclei[19] has been described as "anomalous" in the literature, it will be shown that such a state occurs naturally in the slightly deformed rotor description.

Two collective bands are built on the $\frac{9}{2}^+$ and $\frac{1}{2}^-$ states. The positive-parity band is particularly interesting since it can be compared and contrasted with the decoupled bands observed in Pd nuclei.[1] Unlike the latter, this band has a $\Delta I = 1$ level sequence. Although the $\frac{9}{2}^+$ band is similar to strong-coupled bands observed in strongly deformed nuclei, it has distinct features expected for a slightly deformed nucleus which will be discussed later.

Two additional bands are observed in $^{107}$Ag, one built on the $\frac{17}{2}^-$ state at 2412.0 keV and the other on the $\frac{21}{2}^+$ state at 3148.6 keV. The high-energy band having a negative parity is also observed in $^{105}$Ag. These bands, connected by slightly mixed *M*1-*E*2 transitions, do not appear to be continuations of the bands built on the $\frac{9}{2}^+$ and $\frac{1}{2}^-$ states.

The yrast $\frac{15}{2}^+$ state at 1577.8 keV in $^{107}$Ag does not appear to be part of the band built on the $\frac{9}{2}^+$ state because the $\frac{17}{2}^+$ state feeds the higher-energy $\frac{15}{2}^+$ state at 1799.6 keV in preference to the yrast $\frac{15}{2}^+$ state. The $\Delta I = 2/\Delta I = 1$ branching ratio of the yrast $\frac{15}{2}^+$ state is also opposite to the branching at the other $\frac{15}{2}^+$ and $\frac{11}{2}^+$ states. The yrast $\frac{15}{2}^+$ state is probably isomeric since no transition feeding the state is observed in the coincidence data. Its counterpart in $^{105}$Ag, the $\frac{15}{2}^+$ state at 1734.0 keV, is higher in energy than the $\frac{15}{2}^+$ member of the $\frac{9}{2}^+$ band and is fed by the 579- and 565-keV transitions. Recently this state has been shown to be isomeric.[18]

## IV. ROTATIONAL MODEL CALCULATIONS

A rotational model calculation has been performed to interpret the two bands based on $\frac{9}{2}^+$ and $\frac{1}{2}^-$ states in $^{105,107}$Ag. The calculation of energies and wave functions is the same as that used by Smith and Rickey[2] for Pd nuclei. In addition, the wave functions have been used to calculate electromagnetic transition properties—branching ratios, multipole mixing ratios, and lifetimes. These quantities provide a more stringent test of the model than the energy levels alone. The energy and transition properties of the low-lying $\frac{7}{2}^+$ state are also of great interest.

### A. Calculation of energies and wave functions

The odd-*A* nucleus is treated as a single particle coupled to a slightly deformed even-even core which, to take the simplest case, is axially symmetric in shape. The basis states are strong-coupled rotational states built on single-particle Nilsson states.[20] These are characterized by quantum number *K*, the projection of the total angular momentum $\vec{I}$ on the symmetry axis. As is well known, *K* is equal to $\Omega$, the projection of particle angular momentum $\vec{j}$, because of axial symmetry.

As in Ref. 2, the form of the Coriolis interaction is obtained by expressing the core rotation vector $\vec{R}$ in terms of $\vec{I}$ and $\vec{j}$. The resulting mixing of the basis states is treated by diagonalizing the Hamiltonian. We have also exactly treated the recoil term,

$$\begin{aligned} H_R &= \frac{\hbar^2}{2\mathcal{G}_{IK}}(j^2 - K^2) \\ &= \frac{\hbar^2}{2\mathcal{G}_{IK}} \times \tfrac{1}{2} \times (j_+ j_- + j_- j_+), \end{aligned} \tag{1}$$

where $\mathcal{G}_{IK}$ is the moment of inertia. This term has nonzero diagonal elements for all basis states, and also nondiagonal elements between states having the same value of *K*. The "unperturbed" energies may be expressed as

$$\begin{aligned} E_{IK} = E_K &+ \frac{\hbar^2}{2\mathcal{G}_{IK}}[I(I+1) - K^2 + (\langle j^2\rangle - K^2)] \\ &+ E_C + E_{el}(\mathcal{G}_{IK}), \end{aligned} \tag{2}$$

where the intrinsic energy $E_K$ is obtained from the corresponding Nilsson energy by the usual quasiparticle transformation.[21] $E_C$ is the diagonal contribution of the Coriolis term for the special case $K = \frac{1}{2}$. A variable moment of inertia is used in the calculation as described in Ref. 2. The last term in Eq. (2) is the "elastic energy" included as an extension of the VMI model.[22]

### B. Choice of parameters and results

Separate calculations were not needed for $^{105}$Ag and $^{107}$Ag because they differ only by a pair of neutrons, and the characteristics of the observed states are determined primarily by quasiproton and collective excitations. The expected similarity is evident in the approximate energy

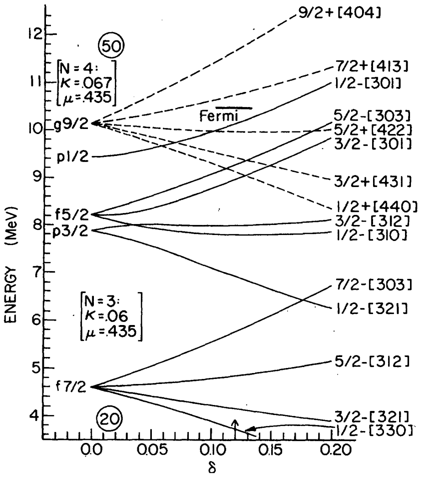

FIG. 5. Nilsson diagram for Ag protons. The Fermi surface is shown as a heavy line. Dashed lines indicate positive parity.

match for corresponding levels in both nuclei.

A number of parameters are involved in the calculation: the $\kappa$ and $\mu$ of the Nilsson model, the deformation $\delta$, the pairing parameters $\lambda$ and $\Delta$, and the VMI parameters[2] $\mathcal{I}_0$ and $C$. All these parameters are constrained by the following considerations. We used $\mu = 0.435$, and $\kappa = 0.06$ (for negative parity, oscillator shell number 3) or 0.067 (for positive parity, oscillator shell number 4). These values give the closest agreement with projected energy levels at zero deformation as listed by Reehal and Sorensen.[23] The resulting Nilsson diagram is shown in Fig. 5. The value of $\delta$ used here was the same as for Pd nuclei,[2] i.e., 0.12. Looking at the Nilsson diagram and considering that Ag has 3 protons less than a complete shell, it is evident that the Fermi surface must be near the $\frac{7}{2}^+[413]$ state. We chose $\lambda = 10.5$ MeV, shown as a heavy horizontal line in Fig. 5. The pairing gap was 1.5 MeV, in accordance with the empirical results described by Bohr and Mottelson.[24] The only Nilsson states included for positive-parity calculations were those arising from the unique-parity $g_{9/2}$ orbital. The negative-parity calculations included the Nilsson states coming from $p_{1/2}$, $f_{5/2}$, and $p_{3/2}$ orbitals. Those from $f_{7/2}$ were also included in preliminary calculations, but the corresponding mixing amplitudes were found to be negligible (less than 0.02). Table III lists the basis states, their energies, quasiparticle energies, occupation probabilities, and $\langle j^2 \rangle$ values.

The VMI parameter $\mathcal{I}_0$ was set equal to zero as in the Pd calculations. The parameter $C$ was $5.2 \times 10^7$ keV$^3$ for all positive-parity bands and $1.2 \times 10^7$ keV$^3$ for the negative-parity bands. These were also comparable to values used for Pd nuclei. Coriolis matrix elements were attenuated by a factor 0.7 following the general trend in strongly deformed nuclei[21] as well as slightly deformed Pd nuclei[2] where such an attenuation is necessary to reproduce the data.

TABLE III. Information on Nilsson states used as basis states for the Coriolis calculations. For positive parity, $\kappa = 0.067$, $\mu = 0.435$; for negative parity, $\kappa = 0.06$, $\mu = 0.435$. $\lambda = 10.5$ MeV and $\Delta = 1.5$ MeV; $\delta = 0.12$.

| Nilsson state | Energy $\epsilon_\Omega$ (keV) | $qp$ energy $E_\Omega$ (keV) | Occupation probability $v^2$ | $\langle j^2 \rangle$ |
|---|---|---|---|---|
| $\frac{1}{2}^+$ [440] | 9 319 | 265 | 0.764 | 24.38 |
| $\frac{3}{2}^+$ [431] | 9 558 | 152 | 0.709 | 24.50 |
| $\frac{5}{2}^+$ [422] | 10 006 | 20 | 0.581 | 24.64 |
| $\frac{7}{2}^+$ [413] | 10 634 | 48 | 0.376 | 24.74 |
| $\frac{9}{2}^+$ [404] | 11 416 | 400 | 0.193 | 24.75 |
| $\frac{1}{2}^-$ [301] | 9 984 | 44 | 0.618 | 0.97 |
| $\frac{1}{2}^-$ [310] | 7 815 | 1445 | 0.931 | 6.91 |
| $\frac{1}{2}^-$ [321] | 7 116 | 2065 | 0.955 | 5.26 |
| $\frac{3}{2}^-$ [301] | 8 776 | 674 | 0.857 | 5.30 |
| $\frac{3}{2}^-$ [312] | 8 002 | 1286 | 0.922 | 7.39 |
| $\frac{5}{2}^-$ [303] | 9 085 | 462 | 0.823 | 8.77 |

The general features of the $^{105,107}$Ag level schemes can be understood even without a detailed Coriolis coupling calculation. Low-energy $\frac{9}{2}^+$, $\frac{7}{2}^+$, and $\frac{1}{2}^-$ states are certainly expected from the Nilsson diagram (Fig. 5). The natural occurrence of the $\frac{7}{2}^+$ state in a slightly deformed rotor description is particularly interesting since there is no simple explanation for such a state in the spherical shell model or in terms of particle-phonon coupling. The general form of collective bands is also transparent. The positive-parity states with low $\Omega$ values are fairly deep into the Fermi sea; therefore, the band built on the $\frac{9}{2}^+$ state will not be decoupled and will have a $\Delta I = 1$ level sequence. The negative-parity states closest to the Fermi surface have small expectation values of $j$; hence, very little Coriolis mixing is expected for negative-parity states.

A Coriolis coupling calculation was performed for a detailed interpretation of the observed decay scheme. Figures 6 and 7 show the calculated energy levels corresponding to positive and negative parities, respectively, together with the experimental energy levels for both isotopes. Some states observed in other experiments[15,18,25] are shown as dashed lines. The overall agreement between the calculated and experimental results is

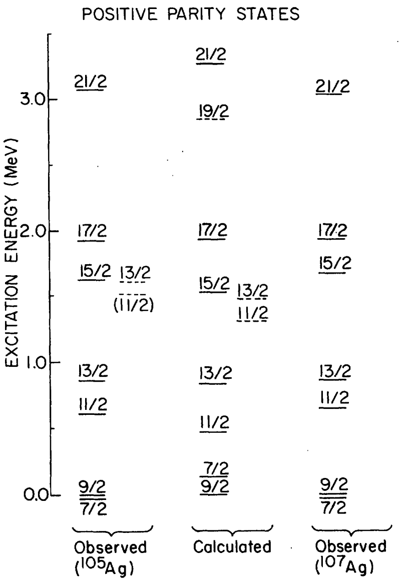

FIG. 6. Comparison of calculated and experimental energies of positive-parity states in $^{105,107}$Ag. Experimental data on states represented by dashed lines have been taken from other works. The energy of the $\frac{9}{2}^+$ state has been subtracted from all energies.

good. The observed $\frac{21}{2}^+$ states in both nuclei are somewhat lower than the calculated energy, but this is probably due to mixing with $\frac{21}{2}^+$ three-quasiparticle states which were not included in the calculation.

It is convenient to classify sets of states in terms of their angular momenta relative to the bandhead angular momentum $I_0$,

$$I = I_0 + n\,,$$

since Coriolis mixing frequently plays a different role in states with $n$ even and states with $n$ odd. We observe a shift in the relative energies of unique-parity $n$-even and $n$-odd states between Pd and Ag nuclei, giving a change from $\Delta I = 2$ bands in Pd to $\Delta I = 1$ in Ag. Since the form and strength of the Coriolis interaction was unchanged, this shift depends only on the position of the Fermi surface.

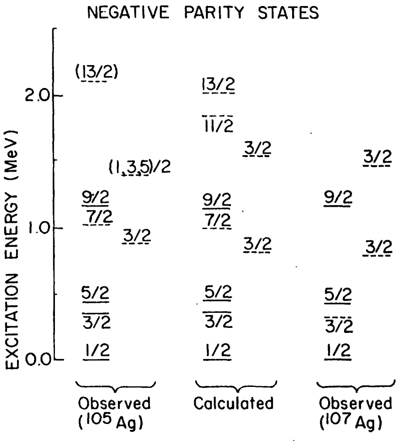

FIG. 7. Comparison of calculated and experimental energies of negative-parity states in $^{105,107}$Ag. Experimental data on states represented by dashed lines have been taken from other works.

A summary of the energies and compositions of the calculated states is given in Table IV. Columns 2, 3, and 4 list the observed energies in $^{105}$Ag and $^{107}$Ag (wherever known), and the corresponding calculated values. The composition of the final states in terms of the 5 basis states (6 in the case of negative parity) is described in as many columns. It is evident that the positive-parity yrast states do not have dominant $K = \frac{1}{2}$ components. Consequently, the positive-parity band is not decoupled. However, there is a considerable mixing, so that the band is not quite strong-coupled either. The contribution to the $n$-even states from low-$K$ (or low-$\Omega$) Nilsson bands increases with increasing spin.

The contributions of various core rotations ($R = 0$, 2, 4, etc.) to each final state have been calculated. The positive-parity states are found to be essentially single-valued in $R$. The $n$-even states have 85 to 96% $R = I - j$ ($j = \frac{9}{2}$), and the $n$-odd states have 99% $R = (I - j) + 1$.

The calculated negative-parity states are also in excellent agreement with the experimental results. There is very little mixing of basis states in the ground-state band, as expected in view of the small values of $I$ and $j$. Table IV shows that this band is dominated by the $\frac{1}{2}$-[301] component, particularly for low spins. The similar energy of pairs of states such as ($\frac{3}{2}^-$, $\frac{5}{2}^-$) and ($\frac{7}{2}^-$, $\frac{9}{2}^-$) is caused by the decoupling parameter which is nearly one ($a = 0.95$).

The identification of a particular calculated state with an observed state is not based solely on energy match, but also on a similarity of decay properties. For example, the calculation predicts two $\frac{7}{2}^-$ states close in energy (930 and 1045 keV). We have shown the latter one in Fig. 7 and Table IV because of its transition properties. The details of these properties will be given in a later subsection.

### C. Calculation of transition properties

The electric and magnetic multipole operators for a single particle in the space-fixed system can be written as[20]

$$\underline{M}_e(\lambda, \mu) = \left[ e_p + (-)^\lambda \frac{Ze}{A^\lambda} \right] r^\lambda Y_{\lambda\mu}(\theta, \varphi)\,, \qquad (3a)$$

TABLE IV. Summary of numerical results of the Coriolis calculation of energy levels and wave functions in $^{105,107}$Ag.

| | Energy (keV) | | | Amount of Coriolis mixing, $f_{IK}^2$ | | | | | |
|---|---|---|---|---|---|---|---|---|---|
| $I$ | $^{105}$Ag | $^{107}$Ag | Calculated | | | | | | |
| | | | | (i) Positive-parity states | | | | | |
| $n$-even states | | | | $\frac{1}{2}^+$[440] | $\frac{3}{2}^+$[431] | $\frac{5}{2}^+$[422] | $\frac{7}{2}^+$[413] | $\frac{9}{2}^+$[404] | |
| $\frac{9}{2}^+$ | ≡0 | ≡0 | ≡0 | 0.03 | 0.07 | 0.17 | 0.34 | 0.38 | |
| $\frac{13}{2}^+$ | 864 | 865 | 839 | 0.15 | 0.22 | 0.27 | 0.25 | 0.11 | |
| $\frac{17}{2}^+$ | 1925 | 1928 | 1947 | 0.22 | 0.29 | 0.28 | 0.16 | 0.05 | |
| $\frac{21}{2}^+$ | 3072 | 3023 | 3248 | 0.27 | 0.32 | 0.26 | 0.12 | 0.03 | |
| $n$-odd states | | | | | | | | | |
| $\frac{7}{2}^+$ | −28 | −33 | 141 | 0.01 | 0.13 | 0.37 | 0.49 | ··· | |
| $\frac{11}{2}^+$ | 616 | 648 | 458 | 0.01 | 0.08 | 0.24 | 0.39 | 0.28 | |
| $\frac{15}{2}^+$ | 1627 | 1674 | 1534 | 0.02 | 0.14 | 0.32 | 0.36 | 0.16 | |
| $\frac{19}{2}^+$ | | | 2844 | 0.03 | 0.19 | 0.36 | 0.32 | 0.10 | |
| Other states | | | | | | | | | |
| $(\frac{11}{2}^+)_2$ | 1519 $^{a,b}$ | | 1256 | 0.04 | 0.26 | 0.23 | 0.00 | 0.47 | |
| $(\frac{13}{2}^+)_2$ | 1613 $^{b}$ | | 1485 | 0.29 | 0.18 | 0.00 | 0.19 | 0.34 | |
| | | | | (ii) Negative-parity states | | | | | |
| $n$-even states | | | | $\frac{1}{2}^-$[301] | $\frac{1}{2}^-$[310] | $\frac{1}{2}^-$[321] | $\frac{3}{2}^-$[301] | $\frac{3}{2}^-$[312] | $\frac{5}{2}^-$[303] |
| $\frac{1}{2}^-$ | ≡0 | ≡0 | ≡0 | 0.99 | 0.00 | 0.01 | ··· | ··· | ··· |
| $\frac{5}{2}^-$ | 433 | 423 | 443 | 0.98 | 0.00 | 0.00 | 0.00 | 0.01 | 0.01 |
| $\frac{9}{2}^-$ | 1166 | 1146 | 1149 | 0.88 | 0.01 | 0.00 | 0.01 | 0.03 | 0.07 |
| $\frac{13}{2}^-$ | 2113 $^{a,b}$ | | 2005 | 0.59 | 0.05 | 0.01 | 0.06 | 0.08 | 0.21 |
| $n$-odd states | | | | | | | | | |
| $\frac{3}{2}^-$ | 347 | 325 $^{b}$ | 356 | 0.98 | 0.01 | 0.00 | 0.00 | 0.01 | ··· |
| $\frac{7}{2}^-$ | 1023 $^{b}$ | | 1045 | 0.94 | 0.02 | 0.00 | 0.02 | 0.01 | 0.01 |
| $\frac{11}{2}^-$ | | | 1901 | 0.88 | 0.04 | 0.00 | 0.06 | 0.02 | 0.00 |
| Other states | | | | | | | | | |
| $(\frac{3}{2}^-)_2$ | 878 $^{b}$ | 786 $^{b}$ | 816 | 0.01 | 0.02 | 0.00 | 0.94 | 0.03 | ··· |
| $(\frac{3}{2}^-)_3$ | 1543 $^{a,b}$ | 1465 $^{b}$ | 1562 | 0.00 | 0.06 | 0.01 | 0.02 | 0.90 | ··· |

[a] Experimental spin-parity assignment is inconclusive.

[b] Energy is known from other sources (Refs. 15, 18, 25).

$$\underline{M}_m(\lambda, \mu) = \frac{e\hbar}{2Mc}\left(g_s\vec{s} + \frac{2}{\lambda+1}g_l\vec{l}\right)\cdot\vec{\nabla}[r^\lambda Y_{\lambda\mu}(\theta, \varphi)], \tag{3b}$$

where $e_p$ is the particle charge (in this case the proton charge), and the coordinates $(r, \theta, \varphi)$ also refer to the particle. The second term within the brackets in (3a) corresponds to the recoil of the nucleus.

The matrix elements of these operators between different strong-coupled states are proportional to the respective transition amplitudes:

$$A_{\text{Nil}}(\lambda, I_iK_i \to I_fK_f) = \left[\frac{8\pi(\lambda+1)}{\lambda\hbar}\right]^{1/2}\frac{1}{(2\lambda+1)!!}\left(\frac{\omega}{c}\right)^{\lambda+1/2} \times (2I+1)^{-1/2}\langle I_fK_f\|\underline{M}(\lambda)\|I_iK_i\rangle, \tag{4}$$

where $\hbar\omega$ is in the transition energy. The electromagnetic *moments* are related to the *diagonal* elements of the matrix, e.g., the electric quadrupole moment is

$$Q(I) \equiv \frac{1}{e}\left\{\frac{16\pi}{5(2I+1)}\right\}^{1/2}\langle II\|\underline{M}_e(E2)\|II\rangle. \tag{5}$$

Nilsson has evaluated these matrix elements by making a transformation to a coordinate system fixed in the nucleus and integrating. The formal results are given in Ref. 20. However, it is more convenient to write the expressions for the transition amplitude for the relevant multipolarities in the form

$$A_{\text{Nil}}(M1, I_i K_i \rightarrow I_f K_f) = 1.03\times 10^6 E_\gamma^{3/2} G_{M1}[C(I_i, 1, I_f; K_i, K_f - K_i) + (-)^{I_f + K_f} b_{M1} C(I_i, 1, I_f; K_i, -K_f - K_i)], \quad (6a)$$

$$\begin{aligned} A_{\text{Nil}}(E1, I_i K_i \rightarrow I_f K_f) = {} & 1.96\times 10^7 (1 - Z/A) A^{1/6} E_\gamma^{3/2} \\ & \times G_{E1}[C(I_i, 1, I_f; K_i, K_f - K_i) + (-)^{I_f + K_f} b_{E1} C(I_i, 1, I_f; K_i, -K_f - K_i)], \end{aligned} \quad (6b)$$

$$\begin{aligned} A_{\text{Nil}}(E2, I_i K_i \rightarrow I_f K_f) = {} & 2.24\times 10^4 (1 + Z/A^2) A^{1/3} E_\gamma^{5/2} \\ & \times G_{E2}[C(I_i, 2, I_f; K_i, K_f - K_i) + (-)^{I_f + K_f} b_{E2} C(I_i, 2, I_f; K_i, -K_f - K_i)], \end{aligned} \quad (6c)$$

where $b_{E\lambda}$ and $G_{E\lambda}$ are functions involving the radial wave functions and the compositions of the initial and final strong-coupled states in the spherical basis. Functions $b_{M\lambda}$ and $G_{M\lambda}$ depend on radial wave functions, compositions of the two Nilsson states, and also the $g$ factors $g_l$ and $g_s$ corresponding to orbital and spin angular momenta. All these functions are independent of $I_i$ and $I_f$. The transition energy $E_\gamma$ is in MeV, and the resulting transition amplitudes are obtained in cgs units.

The collective part of the multipole operator must be included for $M1$ and $E2$ transitions. For $M1$ transitions (which are the only magnetic transitions considered here), the collective effect is small and can be included simply by replacing $g_l$ and $g_s$ by $g_l - g_R$ and $g_s - g_R$, respectively, where $g_R$, the $g$ factor associated with core rotation, is approximately equal to $Z/A$ (Ref. 20).

The collective effects for $E2$ transitions can also be included in a simple way. These effects are present only in intraband transitions which leave the intrinsic part of the wave function unchanged. For intraband $E2$ transitions Eq. (6c) reduces to

$$A_{\text{Nil}}(E2, I_i K_i \rightarrow I_f K_i) = C_0 E_\gamma^{5/2} \cdot G_{E2} C(I_i, 2, I_f; K_i, 0), \quad (7)$$

where $C_0$ is a constant. The $G_{E2}$ factor in the above equation is the quadrupole moment of the single particle, apart from a constant factor. Therefore, collective effects can be included by adding the effect of the quadrupole moment of the core $Q_0$ to $G_{E2}$:

$$G_{E2} \rightarrow G_{E2} + C_1 Q_0 . \quad (8)$$

$C_1$ is readily obtained by a comparison of Eqs. (4), (5), and (6):

$$C_1 = 4.936\times 10^{25} \cdot A^{-1/3},$$

and $Q_0$ can be easily calculated in terms of the deformation parameter. Assuming a Thomas-Fermi charge distribution, Nilsson[20] has obtained

$$Q_0 \approx \tfrac{4}{5} Z R^2 \delta (1 + 2\delta/3), \quad (9)$$

$R$ being the nuclear radius.

Lastly, the states in the nucleus are not pure Nilsson rotational states but *Coriolis-mixed quasiparticle* states. Thus, the correct transition amplitude between states $I_i, I_f$ is

$$\begin{aligned} A(\lambda, I_i \rightarrow I_f) = \sum_{K_i K_f} \{ & f_{I_i K_i} f_{I_f K_f} A_{\text{Nil}}(\lambda, I_i K_i \rightarrow I_f K_f) \\ & \times [u(K_i) u(K_f) \pm v(K_i) v(K_f)] \}, \end{aligned} \quad (10)$$

where the $f_{IK}$'s are the Coriolis mixing amplitudes. The factor within [ ] is the usual pairing correction factor obtained from the quasiparticle transformation, the + sign being used for magnetic and the − sign for electric transitions.[21] Since the collective component of $E2$ is calculated semiempirically, it need not be corrected for quasiparticle effects. It should be noted that if the transition amplitudes are to be obtained with the correct signs, the phases of the Nilsson and the Coriolis mixing amplitudes must be consistent.

The transition probability is just the square of the amplitude,

$$W(\lambda, I_i \rightarrow I_f) = |A(\lambda, I_i \rightarrow I_f)|^2 . \quad (11)$$

The calculation of mixing ratio and reduced transition probability is also straightforward:

$$\delta = \frac{A(E2, I_i \rightarrow I_f)}{A(M1, I_i \rightarrow I_f)}, \quad (12)$$

in the sign convention of Krane and Steffen, and

$$B(\lambda, I_i \rightarrow I_f) = \frac{\lambda[(2\lambda+1)!!]^2 \hbar}{8\pi(\lambda+1)} \times \left(\frac{c}{\omega}\right)^{2\lambda+1} |A(\lambda, I_i \rightarrow I_f)|^2 . \quad (13)$$

### D. Results for $^{105,107}$Ag

In this calculation, we have used Nilsson wave functions, the mixing amplitudes $f_{IK}$, and the occupation parameters $u,v$ as obtained from the calculations already described. The deformation parameter $\delta$ for calculating $Q_0$ was 0.12, as before. *No adjustable parameters were used.*

The results of this calculation for $^{105,107}$Ag are presented in the next two tables. Table V compares the calculated $\gamma$-ray mixing ratios to observed values. The agreement between these, both in magnitude and sign, is quite evident.

Table VI presents the calculated reduced transition probabilities, branching ratios, and half-lives of various states, and compares the last two quantities with their observed counterparts in $^{105,107}$Ag wherever known. The agreement in case of lifetimes (corrected for internal conversion where necessary) is good within a factor of 2–3. The branching ratios (defined as fractions of the total transition probability at the particular level) are also broadly reproduced. The small difference between the observed and calculated branching ratios for $\frac{21}{2}^+$ states is probably because of mixing of the one-quasiparticle and the three-quasiparticle states. The calculation also explains why we do not observe transitions such as $\frac{11}{2}^+ \to \frac{7}{2}^+$, $\frac{21}{2}^+ \to \frac{19}{2}^+$, $\frac{9}{2}^- \to \frac{7}{2}^-$, $\frac{5}{2}^- \to \frac{3}{2}^-$, etc. or parity-changing transitions between any pair of one-quasiparticle states. The correct prediction of mixing ratios, branching ratios, and lifetimes, including those relating to the isomeric state $\frac{9}{2}^+$ and the "anomalous" $\frac{7}{2}^+$ state, with no variable parameter used, is truly remarkable.

TABLE V. $\gamma$-ray mixing ratios in $^{105,107}$Ag calculated using Coriolis mixing. Transition energies used are those observed in $^{107}$Ag, unless otherwise noted.

| $I_i^\pi$ | $I_f^\pi$ | $E_\gamma$ (keV) | Mixing ratio $\delta$ $^{105}$Ag | $^{107}$Ag | Calculated |
|---|---|---|---|---|---|
| $\frac{9}{2}^+$ | $\frac{7}{2}^+$ | 33 [a] | ±0.04(1) [a] | ±0.07(1) [a] | −0.03 |
| $\frac{11}{2}^+$ | $\frac{9}{2}^+$ | 648 | +0.35(4) | +0.33(4) | +0.39 |
| $\frac{13}{2}^+$ | $\frac{11}{2}^+$ | 218 | +0.04(2) | +0.10(5) | +0.06 |
| $\frac{15}{2}^+$ | $\frac{13}{2}^+$ | 809 | +0.25(4) | +0.27(8) | +0.38 |
| $\frac{17}{2}^+$ | $\frac{15}{2}^+$ | 254 | +0.09(4) | | +0.04 |
| $\frac{19}{2}^+$ | $\frac{17}{2}^+$ | 915 [b] | | | +0.40 |
| $\frac{21}{2}^{+}$ [c] | $\frac{19}{2}^+$ | 404 [b] | | | +0.05 |
| $\frac{3}{2}^-$ | $\frac{1}{2}^-$ | 325 [b] | | −0.19(2) [a] | −0.15 |
| $\frac{5}{2}^-$ | $\frac{3}{2}^-$ | 98 [b] | | −0.06(2) [a] | −0.03 |
| $\frac{7}{2}^-$ | $\frac{5}{2}^-$ | 590 [a,d] | +0.02(7) [a] | | −0.07 |
| $\frac{9}{2}^-$ | $\frac{7}{2}^-$ | 143 [a,d] | | | −0.02 |
| $(\frac{3}{2}^-)_2$ | $\frac{3}{2}^-$ | 462 [a] | | −0.01(8) [a] | +0.02 |
| $(\frac{3}{2}^-)_2$ | $\frac{1}{2}^-$ | 786 [a] | | −0.06(1) [a] | −0.01 |

[a] Taken from other sources (Refs. 15,17,19,25).

[b] Transition energy is not known experimentally; calculated value has been used.

[c] We have taken the lower $\frac{21}{2}^+$ state.

[d] Transition energy is that observed in $^{105}$Ag.

The branching and mixing ratios in the $\frac{9}{2}^+$ band show that the $n$-even and $n$-odd states have different characteristics. The $\Delta I = 1$ transitions depopulating the $n$-even states are nearly pure $M1$, whereas the $\Delta I = 1$ transitions originating at $n$-odd states are considerably mixed. The branching ratios always favor transitions to $n$-even states over those to $n$-odd states. This trend is observed even when the transition energies favor the opposite pattern. For example, the $\frac{15}{2}^+$ state decays primarily to the $\frac{13}{2}^+$ $n$-even state although the available energy would favor the transition to the $\frac{11}{2}^+$ $n$-odd state.

These transition properties are very sensitive to the wave functions and are accurately reproduced by the Coriolis calculation. To illustrate the dependence of the wave functions on Coriolis mixing, a calculation, omitting Coriolis mixing, was performed. The contrast between the wave functions from the two calculations can be seen in the reduced transition probabilities shown in Fig. 8. The Coriolis calculation, which agrees with the experimental data, shows that the $B(M1)$ values fluctuate between $n$-even and $n$-odd initial states whereas the $B(E2)$ values show monotonic trends, increasing for $\Delta I = 2$ transitions and decreasing for $\Delta I = 1$ transitions with increasing initial spin $I_i$. When Coriolis mixing is omitted, very different results are obtained; in particular, the dramatic fluctuations of the $B(M1)$ values are not reproduced. This would predict branching ratios for $n$-even states which are the inverse of those observed experimentally.

In Fig. 8(a), we also see, at $I_i = \frac{9}{2}$, one conspicuous exception to the general $B(M1)$ and $B(E2)$ trends for $\Delta I = 1$ transitions as described above. Both probabilities for the $\frac{9}{2}^+ \to \frac{7}{2}^+$ transition are *lower* than those for $\frac{11}{2}^+ \to \frac{9}{2}^+$ transition, and not *higher* as would have been expected from the general trends. This is in excellent agreement with the experimental results and is a significant factor in the long lifetime of the $\frac{9}{2}^+$ state. Without Coriolis mixing the transition probability of $\frac{9}{2}^+ \to \frac{7}{2}^+$ is overestimated by a factor of 20.

## V. DISCUSSION

In the preceding subsection it has been shown that our symmetric rotor calculation is in good

TABLE VI. Branching ratios and life-times in $^{105,107}$Ag calculated using Coriolis mixing. Transition energies used are those observed in $^{107}$Ag, unless otherwise noted.

| | | | $B(E1)$ or $B(M1)$ | $B(E2)$ | Branching ratios | | | Half life (psec) | | |
|---|---|---|---|---|---|---|---|---|---|---|
| $I_i^\pi$ | $I_f^\pi$ | $E_\gamma$ (keV) | (Weisskopf units) | | $^{105}$Ag | $^{107}$Ag | Calculated | $^{105}$Ag | $^{107}$Ag | Calculated |
| $\frac{9}{2}^+$ | $\frac{7}{2}^+$ | 33[a] | 0.026 | 15.4 | ··· | ··· | ··· | $1.8(2)\times10^{3}$[a] | $2.8(1)\times10^{3}$[a] | $2.1\times10^{3}$[b] |
| $\frac{11}{2}^+$ | $\frac{9}{2}^+$ | 648 | 0.07 | 22.5 | 1.00 | 1.00 | 0.94 | | | 0.96 |
| | $\frac{7}{2}^+$ | 681 | ··· | 7.6 | 0.00 | 0.00 | 0.06 | | | |
| $\frac{13}{2}^+$ | $\frac{11}{2}^+$ | 218 | 0.24 | 15.6 | 0.24 | 0.14 | 0.29 | | | 2.52 |
| | $\frac{9}{2}^+$ | 865 | ··· | 10.9 | 0.76 | 0.86 | 0.71 | | | |
| $\frac{15}{2}^+$ | $\frac{13}{2}^+$ | 809 | 0.06 | 12.4 | 0.70 | 0.86 | 0.64 | | | 0.37 |
| | $\frac{11}{2}^+$ | 1026 | ··· | 15.4 | 0.30 | 0.14 | 0.36 | | | |
| $\frac{17}{2}^+$ | $\frac{15}{2}^+$ | 254 | 0.36 | 8.6 | 0.12 | 0.06 | 0.15 | | | 0.56 |
| | $\frac{13}{2}^+$ | 1063 | ··· | 21.3 | 0.88 | 0.94 | 0.85 | | | |
| $\frac{19}{2}^+$ | $\frac{17}{2}^+$ | 915[c] | 0.04 | 6.2 | | | 0.25 | | | 0.17 |
| | $\frac{15}{2}^+$ | 1310[c] | ··· | 21.4 | | | 0.75 | | | |
| $\frac{21}{2}^+$[d] | $\frac{19}{2}^+$ | 404[c] | 0.42 | 5.3 | 0.00 | 0.00 | 0.35 | | | 0.30 |
| | $\frac{17}{2}^+$ | 1095 | ··· | 25.1 | 1.00 | 1.00 | 0.65 | | | |
| $(\frac{11}{2}^+)_2$ | $\frac{9}{2}^+$ | 1520[a,e] | 0.013 | 0.88 | 0.37[a] | | 0.60 | | | 0.36 |
| | $\frac{7}{2}^+$ | 1546[a,e] | ··· | 3.4 | 0.63 | | 0.40 | | | |
| | $\frac{13}{2}^+$ | 748[a,e] | 0.011 | 1.8 | 0.21[a] | | 0.23 | | | |
| $(\frac{13}{2}^+)_2$ | $\frac{11}{2}^+$ | 997[a,e] | 0.007 | 6.1 | 0.57 | | 0.61 | | | 1.38 |
| | $\frac{9}{2}^+$ | 1612[a,e] | ··· | 0.29 | 0.22 | | 0.16 | | | |
| $\frac{3}{2}^-$ | $\frac{1}{2}^-$ | 325[a] | 0.13 | 17.9 | ··· | ··· | ··· | | 5.2(9)[a] | 4.77 |
| $\frac{5}{2}^-$ | $\frac{3}{2}^-$ | 98[a] | 0.11 | 4.75 | 0.05[a] | 0.04[a] | 0.24 | | 40(3)[a] | 57.86 |
| | $\frac{1}{2}^-$ | 423 | ··· | 17.5 | 0.95 | 0.96 | 0.76 | | | |
| | $\frac{5}{2}^-$ | 590[a,e] | 0.21 | 2.55 | 0.71[a] | | 0.92 | | | |
| $\frac{7}{2}^-$ | $\frac{3}{2}^-$ | 677[a,e] | ··· | 22.3 | 0.29 | | 0.08 | | | 0.47 |
| | $\frac{7}{2}^+$ | 998[a,e] | $1.2\times10^{-6}$ | ··· | 0.00 | | 0.00 | | | |
| | $\frac{7}{2}^-$ | 143[a,e] | 0.07 | 0.06 | 0.00 | 0.00 | 0.02 | | | |
| $\frac{9}{2}^-$ | $\frac{5}{2}^-$ | 723 | ··· | 24.1 | 1.00 | 1.00 | 0.98 | | | 3.77 |
| | $\frac{9}{2}^+$ | 1020 | $2.2\times10^{-8}$ | ··· | 0.00 | 0.00 | 0.00 | | | |
| | $\frac{7}{2}^+$ | 1052 | $2.3\times10^{-8}$ | ··· | 0.00 | 0.00 | 0.00 | | | |
| $\frac{11}{2}^-$ | $\frac{9}{2}^-$ | 736[c] | 0.25 | 0.74 | | | 0.88 | | | 0.20 |
| | $\frac{7}{2}^-$ | 841[c] | ··· | 26.9 | | | 0.12 | | | |
| $\frac{13}{2}^-$ | $\frac{11}{2}^-$ | 101[c] | 0.02 | 0.09 | 0.00[a] | | 0.00 | | | 0.92 |
| | $\frac{9}{2}^-$ | 947[e] | ··· | 26.2 | 1.00 | | 1.00 | | | |
| | $\frac{5}{2}^-$ | 364[a] | 0.10 | 0.25 | 0.00[a] | 0.08[a] | 0.01 | | | |
| $(\frac{3}{2}^-)_2$ | $\frac{3}{2}^-$ | 462[a] | 0.51 | 0.83 | 0.24 | 0.28 | 0.15 | | 0.27(8)[a] | 0.09 |
| | $\frac{1}{2}^-$ | 786[a] | 0.59 | 0.02 | 0.76 | 0.64 | 0.84 | | | |
| | $\frac{5}{2}^-$ | 983[a] | 0.02 | 0.04 | 0.00[a] | 0.00[a] | 0.11 | | | |
| $(\frac{3}{2}^-)_3$ | $\frac{3}{2}^-$ | 1069[a] | 0.07 | 0.02 | 0.00 | 1.00 | 0.41 | | <0.6[a] | 0.11 |
| | $(\frac{3}{2}^-)_2$ | 575[a] | 0.02 | 0.07 | 0.00 | 0.00 | 0.02 | | | |
| | $\frac{1}{2}^-$ | 1416[a] | 0.03 | 0.002 | 1.00 | 0.00 | 0.46 | | | |

TABLE VI. (*Continued*)

---

[a] Taken from other sources (Refs. 15,18,19,25).

[b] The half-life has been corrected for internal conversion.

[c] Transition energy is not known experimentally; calculated value has been used.

[d] We have considered the lower $\frac{21}{2}^{+}$ state.

[e] The transition energy is that observed in $^{105}$Ag.

agreement with the energies and decay properties of many states in $^{105,107}$Ag. A different rotational interpretation has been given for positive-parity states by Kalshoven *et al.* In a recent publication,[18] they have shown that many energy levels, branching ratios, and mixing ratios in $^{105}$Ag can be reproduced by the triaxial rotor model of Meyer-ter-Vehn.[26] However, the results obtained with the extra degree of freedom in the triaxial model are in no better agreement with experiment than those obtained here. The large value of the deformation parameter used in the triaxial calculation ($\beta=0.23$ compared to $\beta\approx\delta=0.12$ in our calculation) is somewhat surprising since there is no evidence of such a sizable deformation in this region of nuclei. The value of $\gamma$ used was also large, 22°. In our calculation the smaller deformation is required to reproduce the observed $E2$ transition properties. The microscopic calculations of Nerlo-Pomorska *et al.*[27] predict a small symmetric deformation for $^{103,105}$Ag ($\beta=0.1$ to 0.15; $\gamma=0°$) in agreement with our parameters. It is noteworthy that some states are reproduced by neither the axial nor the triaxial model, e.g., the nonyrast $\frac{15}{2}^{+}$ and $\frac{17}{2}^{+}$ states in $^{105}$Ag.

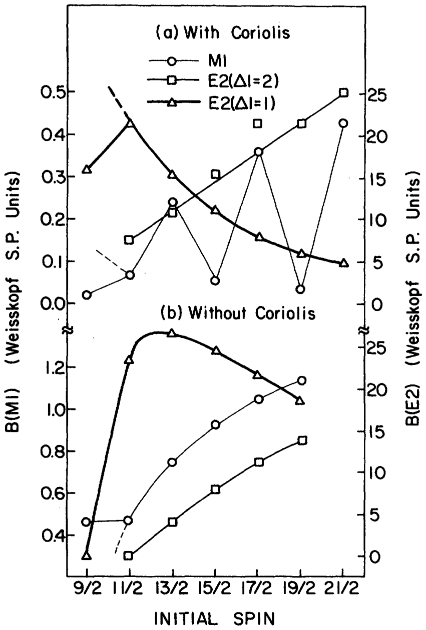

FIG. 8. Calculated values of reduced transition probabilities $B(E2)$ and $B(M1)$ in $^{105,107}$Ag, (a) using Coriolis-mixed wave functions and (b) without Coriolis mixing.

A group of states are observed in $^{105,107}$Ag at energies above 2.3 MeV, which represent a departure from the predicted one-quasiparticle structure. These states fall into bands built on high-spin bandheads ($I^{\pi}=\frac{21}{2}^{+}$ and $\frac{17}{2}^{-}$), which we suggest are three-quasiparticle states. In neighboring even-even Pd and Cd nuclei, states with comparable energies have been interpreted[4] as two-quasiparticle states. The angular momenta of the intruder states in $^{105,107}$Ag can easily be obtained by coupling one quasiproton to the observed two-quasiparticle states. For example, an $8^{+}$ state of $(g_{9/2})^2$ parentage has been observed in Pd and Cd nuclei. By coupling a $g_{9/2}$ quasiproton to this state a $\frac{21}{2}^{+}$ bandhead could be obtained, and coupling a $p_{1/2}$ quasiproton could produce $\frac{15}{2}^{-}$ and $\frac{17}{2}^{-}$ states. A positive identification of these states, however, would require a three-quasiparticle calculation. These intruder states are not unique to Ag nuclei but have also been observed in all odd-$A$, mass-100 nuclei where high-spin states have been investigated.

One of the major reasons for studying $^{105,107}$Ag was that a $\Delta I=1$ band involving the unique-parity $g_{9/2}$ orbital was expected because the position of the Fermi level was near high $\Omega$ values. Although the expected band was observed, the large amount of Coriolis mixing in the band was unexpected.

Accepted ideas about rotation alignment would imply that Coriolis mixing becomes smaller as the Fermi surface moves to higher values of $\Omega$. The discussion of the concepts is complicated because of the large off-diagonal Coriolis matrix elements. However, we can use the final Coriolis-mixed wave function to define quantities which convey independently the degree of alignment of the state and the Coriolis energy. Then in terms of these parameters the effects of the Coriolis interaction on the predicted nuclear structure can be examined.

For given values of $R$ and $j$ the possible values of total angular momentum $I$ can be obtained from the scalar equation

$$I=R+j-\alpha\,, \tag{14}$$

where $\alpha$ is an integer which can vary from 0 to

$2j$ or $2R$, whichever is smaller. The most aligned coupling corresponds to that of minimum $\alpha$. In general neither $R$ nor $j$ is a good quantum number, but the positive parity bands present in Ag contain the single value of $j=\frac{9}{2}$. For a given value of $R$ the degree of alignment can be expressed as

$$\frac{I-R}{j}=\frac{j-\alpha}{j},$$

which varies between the limits of +1 and −1. There are still a range of $R$ values allowed for each final state, but the fractional composition, $P(I,M,R)$, of each state in terms of the allowed $R$ is routinely calculated. Thus the normalized differences defined above can be summed over allowed $R$, weighted by the appropriate $P(I,M,R)$, to give a parameter $D(I,M)$ which describes the degree of alignment of the state:

$$D(I,M)=\sum_R P(I,M,R)\frac{(I-R)}{j}. \tag{15}$$

It is clear that, since $R$ can have only even values, not all states can have perfect alignment corresponding to $D(I,M)=+1$. The positive-parity $n$-odd states discussed in the present work must have $\alpha$'s of at least one, so that the maximum possible value of $D(I,M)$ for these states is 0.77.

With this parametrization the alignment of states in the $\frac{9}{2}^+$ band can be calculated. The $n$-even states are found to have values of $D(I,M)$ ranging from 0.93 to 0.98, with increasing spin. The $n$-odd states all have essentially the same value of $D(I,M)=0.77$. This rather surprising result shows that all of the states in this $\Delta I=1$ band exhibit nearly maximal alignment, which destroys the notion that the shift from $\Delta I=2$ to $\Delta I=1$ bands is caused by a decrease in alignment as the Fermi surface moves to higher values of $\Omega$.

A different way to parametrize the results of the model calculation is to evaluate the effects on final energies of the Coriolis interaction. This cannot be done in the usual strong-coupled basis since Coriolis matrix elements are nondiagonal in this representation. This effect must be evaluated using the final Coriolis-mixed eigenfunction of the total Hamiltonian.

The total Hamiltonian is, in the usual fashion, separated into two parts,

$$H=H_0+H_{\mathrm{ND}}. \tag{16}$$

$H_0$ contains all of the operators which are diagonal in the strong-coupled basis, i.e.,

$$H_0\varphi_{IMK}=E_{IMK}\varphi_{IMK},$$

and the diagonal Coriolis and recoil terms are explicitly included. $H_{\mathrm{ND}}$ contains nondiagonal terms from the Coriolis and recoil operators. The eigenfunctions of the total Hamiltonian are expressed as linear combinations of the basis states

$$\Psi_{IM}=\sum_K f_{IMK}\varphi_{IMK}, \tag{17}$$

where the $f_{IMK}$ are the Coriolis mixing amplitudes. Neither part of the total Hamiltonian is individually diagonal in the $\Psi_{IM}$ basis, but expectation values can be calculated.

We define

$$E_{ID}=\langle\Psi^*_{IM}|H_0|\Psi_{IM}\rangle \tag{18a}$$

and

$$E_C=\langle\Psi^*_{IM}|H_{\mathrm{ND}}|\Psi_{IM}\rangle. \tag{18b}$$

It should be noted that $E_{ID}$ is a weighted sum of the original diagonal energies $E_{IK}$:

$$E_{ID}=\sum_K f_{IMK}{}^2E_{IK}. \tag{19}$$

Neither of these two parameters is separately measurable as an energy, and only the sum is an observable quantity, but they are useful in discussing the role of Coriolis forces under different circumstances.

In order to study the transition from $\Delta I=2$ to $\Delta I=1$ bands we have performed additional Coriolis mixing calculations in two limiting cases. The first, which will be referred to as the "decoupled" case, placed the Fermi surface below all $g_{9/2}$ Nilsson orbitals. The second, or "strong-coupled" case, placed the Fermi surface above all $g_{9/2}$ Nilsson orbitals. As expected, the first calculation yielded a definite $\Delta I=2$ band, while the second gave a smooth $\Delta I=1$ band with the general characteristics of a $K=\frac{9}{2}$ Nilsson band. The parameters $E_{ID}$ and $E_C$ were calculated for final states in these cases as well as for the results of the actual $^{105,107}$Ag calculation (which is referred to as the "intermediate" case). This analysis is shown in Fig. 9. Part (a) shows the variation with spin of $E_C$, and part (b) shows the variation of $E_{ID}$. (In order to show the fluctuations clearly, these energies are normalized by dividing them by $I$.) It should be noted that $E_{ID}$ contains the Coriolis energy due to the contribution of the decoupling parameter in the $K=\frac{1}{2}$ band, which is separately plotted in part (c). It is seen that the behavior and magnitude of the "Coriolis energy" $E_C$ in the intermediate case is very similar to that in the decoupled case, and is not responsible for the shift from $\Delta I=2$ to $\Delta I=1$ bands. The primary reason for the $\Delta I=2$ nature of the decoupled band is seen to be the large component of the $K=\frac{1}{2}$ Nilsson state in the wave

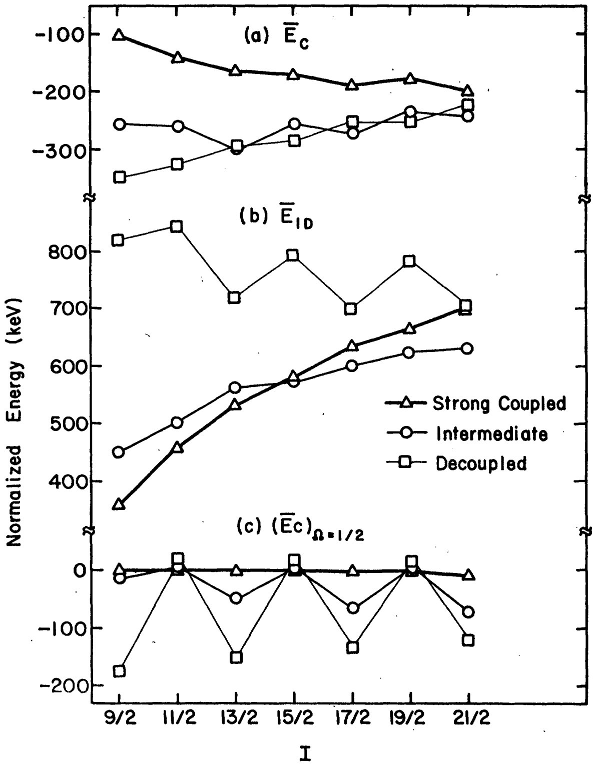

FIG. 9. Systematics of the energy contributions (a)$E_{ID}$, (b) $E_C$, and (c) $(E_C)_{\Omega=1/2}$ for the decoupled, intermediate, and strong-coupled cases. The energies have been normalized by dividing them by $I$.

functions, which has a dramatic effect on the "diagonal energies" $E_{ID}$. The energies of alternate states in a $K=\frac{1}{2}$ band are modified from the usual smooth rotational pattern by diagonal Coriolis energies

$$(E_C)_{K=1/2} = \frac{\hbar^2}{2\mathcal{J}} a(-1)^{I+1/2}(I+1/2)\,, \tag{20}$$

where $a$ is the decoupling parameter[28] defined as

$$a = -\sum_j (-1)^{j+1/2}(j+\tfrac{1}{2})|Cjl|^2\,. \tag{21}$$

There are significant aspects of these equations for a single $j$ shell which are independent of the value of $j$. First, the sum over $j$ in Eq. (21) vanishes, so that the decoupling parameter is

$$a = -(-1)^{j+1/2}(j+\tfrac{1}{2})\,.$$

Second, the diagonal Coriolis energy of Eq. (20) is always negative for states with $I=j$, $j+2$, etc.,

$$\begin{aligned} a(-1)^{I+1/2} &= -(-1)^{j+1/2}(j+\tfrac{1}{2})(-1)^{I+1/2} \\ &= -(-1)^{2j+1}(j+\tfrac{1}{2}) \\ &= (-1)(j+\tfrac{1}{2})\,. \end{aligned}$$

Third, the energy difference between successive states follows a distinct pattern:

$$\begin{aligned} \frac{2\mathcal{J}}{\hbar^2}(E_I - E_{I-1}) &\cong I(I+1) + (-1)^{I+1/2}a(I+\tfrac{1}{2}) \\ &\quad - (I-1)(I) - (-1)^{I-1/2}a(I-\tfrac{1}{2}) \\ &= 2I[1+a(-1)^{I+1/2}]\,. \end{aligned}$$

Realizing that $I_0=j$, the energies in the $K=\frac{1}{2}$ bands of $n$-even states relative to $n$-odd states of the next lower spin are thus seen to be

$$\frac{2\mathcal{J}}{\hbar^2}(E_I - E_{I-1}) = 2I[1-(j+\tfrac{1}{2})]\,. \tag{22}$$

This energy difference would give rise to a $\Delta I=2$ band for all $j$, and the difference increases as $j$ becomes larger.

Our analysis shows that the relative amount of the $K=\frac{1}{2}$ band in the final wave function is in fact the controlling factor in the difference between the $\Delta I=2$ and the $\Delta I=1$ bands. As the Fermi surface moves to intermediate values of $\Omega$ the $\Delta I=2$ character of the band disappears because the $K=\frac{1}{2}$ band moves to higher energies. But the "Coriolis energy" $E_C$ remains large, as is seen in Fig. 9(a), even when the Fermi surface lies near high $\Omega$ values. The Coriolis mixing causes the energies and transition properties to be distinctly different from the strong-coupling limit. The Coriolis energy becomes small only when the Fermi surface is well above the highest $\Omega$ values and the observed structure then resembles the strong-coupling limit. Even in this case, the Coriolis energy increases at high spins and cannot be entirely neglected.

In light of the previous discussion, the alignment factors $D(I,M)$ can be better understood. These factors for the three cases are given in Table VII. For the decoupled and intermediate cases the alignment parameters for the $n$-even states are not significantly different. There is a trend for the alignment of the $n$-odd states to *increase* as the Fermi surface moves to intermediate $\Omega$ values. It is only when the Fermi surface is above the highest $\Omega$ values that alignment of all states decreases, but still remains substantial.

This analysis can be summarized with the observation that the Coriolis interaction does all that it can to maximize alignment in the yrast states, but alignment does not dictate the $\Delta I=2$ or the $\Delta I=1$ nature of bands. That is decided almost solely by the position of the $\Omega=\frac{1}{2}$ state relative to the Fermi surface.

## VI. CONCLUSIONS

The level schemes of $^{105,107}$Ag are seen to be in good agreement with a rotational calculation which

TABLE VII. Rotation-alignment parameter systematics in the band built on the unique-parity $g_{9/2}$ orbital.

| Spin $I$ | Alignment parameter $D$ Decoupled | Intermediate | Strong-coupled |
|---|---|---|---|
| $n$-even states | | | |
| $\frac{9}{2}$ | 0.87 | 0.93 | 0.725 |
| $\frac{13}{2}$ | 0.95 | 0.96 | 0.68 |
| $\frac{17}{2}$ | 0.97 | 0.97 | 0.73 |
| $\frac{21}{2}$ | 0.973 | 0.98 | 0.80 |
| $n$-odd states | | | |
| $\frac{11}{2}$ | 0.66 | 0.77 | 0.66 |
| $\frac{15}{2}$ | 0.70 | 0.77 | 0.67 |
| $\frac{19}{2}$ | 0.72 | 0.77 | 0.69 |

treats these nuclei as slightly deformed symmetric rotors. This agreement includes not only energy levels but transition properties as well. The dominant features observed in both nuclei follow naturally in this description, which lends weight to the opinion that the rotational description is not confined to strongly deformed rare-earth nuclei but applies to nuclei in region $A \approx 100$ also.

The level schemes of Ag nuclei, which have a core very similar to that of the neighboring Pd nuclei, look very different from the latter. In particular, the collective band based on the unique-parity $h_{11/2}$ orbital in Pd has a $\Delta I = 2$ level sequence, whereas its counterpart in Ag has a $\Delta I = 1$ sequence. However, the same rotational calculation that reproduced the energy levels in Pd also predicts the levels in Ag nuclei. Since the form and strength of the Coriolis interaction is explicitly defined in our model, the only essential difference between the parameters used in the two cases is the Fermi level. But this difference follows simply from the number of protons in the Ag nuclei and is not imposed arbitrarily. Hence the success of the calculation in both cases implies the general applicability of the model in this region of nuclei.

We have also studied the effects of the position of the Fermi surface on rotation alignment. We find that the Coriolis interaction maximizes alignment in the yrast states even when the Fermi surface lies near Nilsson states of relatively high $\Omega$ values. The primary factor which produces $\Delta I = 2$ bands is the relative positions of $n$-even and $n$-odd states in the $\Omega = \frac{1}{2}$ band, which are strongly altered from the natural rotational sequence by the action of the Coriolis decoupling parameter. Therefore, the occurrence of a $\Delta I = 2$ sequence in yrast states is governed by the magnitude of the decoupling parameter and the position of the $\Omega = \frac{1}{2}$ state relative to the Fermi surface.

This work was supported by the National Science Foundation.

---

*Present address: Schlumberger-Doll Research Center, P. O. Box 307, Ridgefield, Connecticut 06877.

†Present address: Texas Instruments, Inc., Dallas, Texas.

‡Present address: Nuclear Physics Laboratory, University of Colorado, Boulder, Colorado 80304.

[1] F. A. Rickey, J. A. Grau, L. E. Samuelson, and P. C. Simms, Phys. Rev. C 15, 1530 (1977).

[2] H. A. Smith, Jr. and F. A. Rickey, Phys. Rev. C 14, 1946 (1976).

[3] J. A. Grau, L. E. Samuelson, S. I. Popik, F. A. Rickey, and P. C. Simms (unpublished).

[4] L. E. Samuelson, J. A. Grau, S. I. Popik, F. A. Rickey, and P. C. Simms, Phys. Rev. C 19, 73 (1979).

[5] A. K. Kerman, Dan. Mat. -Fys. Medd. 30, No. 15 (1956).

[6] R. K. Popli, J. A. Grau, L. E. Samuelson, F. A. Rickey, and P. C. Simms (unpublished).

[7] J. A. Grau, L. E. Samuelson, F. A. Rickey, P. C. Simms, and G. J. Smith, Phys. Rev. C 14, 2297 (1976).

[8] W. Klamra and J. Rekstad, Nucl. Phys. A258, 61 (1976).

[9] R. L. Robinson, F. K. McGowan, P. H. Stelson, W. T. Milner, and R. O. Sayer, Nucl. Phys. A124, 553 (1969).

[10] L. -G. Svensson, O. Bergman, A. Bäcklin, N. -G. Jonsson, and J. Lindskog, Internal Report No. UUIP-904, Uppsala University, 1975 (unpublished).

[11] J. A. Grau, Z. W. Grabowski, F. A. Rickey, P. C. Simms, and R. M. Steffen, Phys. Rev. Lett. 32, 667 (1974).

[12] J. A. Grau, F. A. Rickey, G. J. Smith, P. C. Simms, and J. R. Tesmer, Nucl. Phys. A229, 346 (1974).

[13] P. C. Simms, G. J. Smith, F. A. Rickey, J. A. Grau, J. R. Tesmer, and R. M. Steffen, Phys. Rev. C 9, 684 (1974).

[14] T. Yamazaki, Nucl. Data A3, 1 (1967).

[15] R. L. Robinson, F. K. McGowan, P. H. Stelson, and W. T. Milner, Nucl. Phys. A150, 225 (1970).

[16] R. S. Hager and E. C. Seltzer, Nucl. Data A4, 1 (1968).

[17] D. Hippe, H. -W. Schuh, B. Heits, A. Rademacher, K. -O. Zell, P. v. Brentano, J. Eberth, and E. Eube, Z. Phys. A284, 329 (1978).

[18] A. W. B. Kalshoven, W. H. A. Hesselink, T. J. Ketel, J. Ludziejewski, L. K. Peker, J. J. Van Ruyven, and H. Verheul, Nucl. Phys. A315, 334 (1979).

[19] L. -G. Svensson, O. Bergman, A. Bäcklin, N. -G. Jonsson, and J. Lindskog, Phys. Scripta 14, 129 (1976); P. D. Bond, E. C. May, and S. Jha, Nucl. Phys. A179, 389 (1972); C. Bergman, B. Svahn, L. -G. Svensson, A. Bäcklin, and J. Lindskog, *ibid.* 223, 342 (1974).

[20] S. G. Nilsson, Dan. Mat. -Fys. Medd. 29, No. 16 (1955).

[21] M. E. Bunker and C. W. Reich, Rev. Mod. Phys. 43, 348 (1971).

[22] M. A. J. Mariscotti, G. Scharff-Goldhaber, and B. Buck, Phys. Rev. 178, 1864 (1969).

[23] B. S. Reehal and R. Sorensen, Phys. Rev. C 2, 819 (1970).

[24] A. Bohr and B. R. Mottelson, *Nuclear Structure* (Benjamin, New York, 1969), Vol. I, p. 170.

[25] S. V. Jackson, W. B. Walters, and R. A. Meyer, Phys. Rev. C 13, 803 (1975).

[26] J. Meyer-ter-Vehn, Nucl. Phys. A249, 111 (1975); A249, 141 (1975).

[27] B. Nerlo-Pomorska and J. Ludziejewski, Z. Phys. A287, 337 (1978).

[28] M. A. Preston, *Physics of the Nucleus* (Addison-Wesley, Reading, Massachusetts, 1962) p. 258.